Cement and Concrete Composites 144 (2023) 105281

Contents lists available at ScienceDirect

Cement and Concrete Composites

journal homepage: www.elsevier.com/locate/cemconcomp

Carbonation and self-healing in concrete: Kinetic Monte Carlo simulations of mineralization

Aleena Alex [a,*], Brubeck Freeman [b,c], Anthony Jefferson [c], Enrico Masoero [c,d]

[a] Newcastle University, Claremont Road, NE1 7RU, Newcastle upon Tyne, United Kingdom
[b] LUSAS, Forge House, 66 High Street, Kingston upon Thames, Surrey, KT1 1HN, United Kingdom
[c] Cardiff University, Queens Buildings, The Parade, CF24 3AA, Cardiff, United Kingdom
[d] Politecnico di Milano, Piazza Leonardo da Vinci, 32, 20133, Milano, MI, Italy

A B S T R A C T

Industrial applications of carbonation such as self-healing and carbon capture and storage have been limited, due to a lack of reliable predictive models linking the chemistry of carbonation at the molecular scale to microstructure development and macroscopic properties. This work proposes a coarse-grained Kinetic Monte Carlo (KMC) approach to simulate microstructural evolution of a model cement paste during carbonation, along with evolution of pore solution chemistry and saturation indexes of solid species involved. The simulations predict the effective rate constants for $Ca(OH)_2$ dissolution and $CaCO_3$ precipitation as $k_{Ca(OH)2} = 2.20 \times 10^{-5}$ kg/m^3/s and $k_{CaCO3} = 4.24 \times 10^{-6}$ kg/m^3/s. These values are directly fed to a macroscale reactive transport model to predict carbonate penetration depth. The rate constants from the molecular scale are used in a boundary nucleation and growth model to predict self-healing of cracks. Subsequently these results are compared with experimental data, and provide good agreement. This proposed multiscale approach can help understand and manage the carbonation of both traditional and new concretes, supporting applications in residual lifetime assessment, carbon capture, and self-healing.

1. Introduction

Carbonation in hardened, Ordinary Portland Cement (OPC) pastes refers to the dissolution of hydrates releasing calcium ions into solution, which react with dissolved carbonates to produce $CaCO_3$ [1]. Excessive carbonation lowers the pH of the pore solution, causing disintegration of hydration products, corrosion of reinforcing steel, and ultimately cracks that reduce the durability of a structure [2–4]. In some cases, carbonation also favours the penetration of chlorides into concrete, which further deteriorates the structure [5,6]. However, when properly directed and controlled, carbonation can be beneficial for applications such as carbon capture and storage (CCS) and self-healing concrete (SHC).

In CCS, concrete is cured in a CO_2 rich atmosphere [7,8] using CO_2 that was previously captured at the point source [9–11]. This leads to unconventional concretes that are rich in carbonate minerals, for which it is challenging to ensure satisfactory performance while still preserving environmental benefits (e.g. not adding more OPC to compensate for strength losses) [12]. SHC instead aims at increasing the durability of concrete structures, thus reducing the environmental footprint of cement production, which currently causes 7-8% of the global anthropogenic CO_2 emissions [13]. Crack formation in concrete enables the ingress of water and dissolved CO_2, which can be exploited to trigger autogenous or autonomous self-healing. In autogenous self-healing, unreacted oxides (e.g. belite, C_2S) and other soluble phases (e.g. calcium hydroxide) undergo delayed dissolution in aged concrete after cracking; the dissolved ions form new hydration products, such as C-S-H or $CaCO_3$, sealing the cracks. In autonomous self-healing, sealing agents are encapsulated in the cement matrix, e.g. bacteria [14], enzymes [15] or other sealing substances [16]. These become active when cracks and moisture ingress change the local exposure conditions, triggering chemical reactions and forming new phases that ultimately seal the cracks (e.g. $CaCO_3$ from enzymatic self-healing in Fig. 1). Microbial Induced Carbonate precipitation (MICP) and biomineralization is of particular interest in autonomous healing SHC applications [17–22]. The interested reader can find a review on the modelling possibilities of MICP and its challenges in Ref. [23]. SHC typically restores the low, original permeability of concrete, but issues persist especially due to residual strength loss after $CaCO_3$ precipitation and, in some cases, a lowering of the pH that favours the corrosion of the reinforcement. Applications of both CCS and SHC are still largely empirical and would benefit from a better understanding of how the mineralization process and the possible use of admixtures might be fine-tuned to ensure performance. Predictive models would be particularly useful for the

* Corresponding author.
E-mail addresses: aleena.alex@newcastle.ac.uk (A. Alex), brubeck.freeman@lusas.com (B. Freeman), jeffersonad@cardiff.ac.uk (A. Jefferson), masoeroe@cardiff.ac.uk, enrico.masoero@polimi.it (E. Masoero).

https://doi.org/10.1016/j.cemconcomp.2023.105281
Received 14 April 2023; Received in revised form 24 August 2023; Accepted 2 September 2023
Available online 6 September 2023

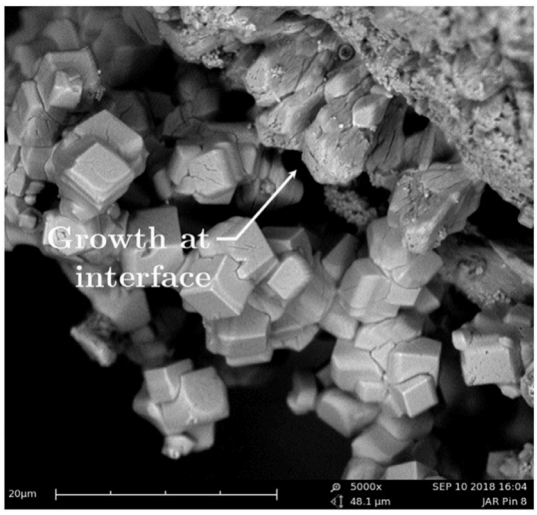

Fig. 1. Reproduced from Rosewitz et al. [15] showing the crystalline $CaCO_3$ growth at the solid-water interface i.e. the crack surface.

adoption of new concretes based on unconventional cements, with lower embodied carbon and energy than OPC, but for which there is little if any experimental data on long-term changes during carbonation.

Analytical and numerical models of carbonation and self-healing in OPC-based concretes are relatively abundant at the macroscale. Papadakis et al. [24] proposed a physiochemical model based on diffusion kinetics, describing the progression of the carbonation front in concrete samples. Saetta et al. [25] developed a distributed parameter model for the carbonation of calcium hydroxide (CH in cement notation [26]) in the pore structure of concrete, which describes the spatial and temporal evolution of heat, moisture, CO_2 consumption, and the reduction in porosity due to $CaCO_3$ deposition. Chitez et al. and Freeman et al. [27,28] proposed a model of reactive transport that simulates the early-stage autogenous healing of regular cement-based materials. The primary healing mechanisms considered in the model were the hydration of unreacted cement particles and carbonation. However, all these macroscale models rely on heuristic constitutive assumptions; in particular, reaction rates are often described using effective rate constants that summarize the complex result of multiple microstructural details and processes, such as eigenstress evolution, relative volume fraction and specific surface area of various solid phases, and chains of individual chemical reactions. Macroscale models do not resolve these details, hence they employ effective rate constants that are empirically calibrated to fit experimental data; this is clearly limiting the predictive ability of the simulations, especially when dealing with new material chemistries. As a result, the current state of the art in macroscale simulations features the ability to fit, but not to predict, typical experimental data such as those on carbonation depth shown in Fig. 2.

An alternative approach would be to inform the macroscale models using constitutive laws obtained from more detailed simulations at the microstructural level. Ab initio and molecular simulations would be the fundamental starting point to produce such laws, but they cannot yet cover the complexity and large length and time scales of the processes at play during carbonation; indeed, the few existing applications of such simulations to concrete carbonation are still returning conflicting results, e.g. on the beneficial or detrimental role of water during carbonation [30,31]. The need for dedicated mesoscale models, to bridge the gap between molecular, microstructural, and macroscale models, is well recognized, including in the concrete modelling community [32]. For carbonation, however, there are currently no mesoscale simulations describing how chemical reactions and internal stresses together drive the evolution of microstructure and strength in concrete.

This paper presents coarse-grained, mesoscale, particle-based simulations of carbonation in a cement paste, using a recently developed Kinetic Monte Carlo (KMC) framework that accounts for both slow chemical reactions and mechanical interactions. The interested reader can refer to Ref. [23] for a discussion of the new capabilities that this KMC framework offers, for simulating autogenous and autonomous self-healing systems, both pivoted on the carbonation process. A simulation cell containing C-S-H gel and crystalline CH is modelled and the interaction potentials between solid particles are parameterized. The pore solution is modelled through the concentration values of relevant species, such as Ca^{2+}, OH^{-}, CO_3^{2-} etc. During the simulations, particles of C-S-H and CH dissolve while $CaCO_3$ particles precipitate based on rate equations that are derived from fundamental Transition State Theory (TST). The simulations predict microstructural evolution during carbonation as well as the effective reaction rate constants of CH dissolution and $CaCO_3$ precipitation, which depend on the evolving microstructural morphology and chemical environment in the system. These effective rate constants are applied in a macroscale reactive transport model, predicting the experimental data on carbonation depth from Fig. 2. In addition to this, the rate constants for $CaCO_3$ precipitation from molecular scale are fed into a new boundary nucleation and growth model (BNG) for predicting carbonation based self-healing of cracks. All this outlines a multiscale modelling approach that can now be exploited to simulate self-healing, CCS, and deterioration of concrete during carbonation, both when traditional OPC and when new and unconventional cements are used.

2. Methodology

This work examines the carbonation and autogenous healing of a fully hydrated, model cement paste, containing only calcium silicate hydrate (C-S-H) and calcium hydroxide (CH) and without any added self-healing agent (only CO_2 from the atmosphere). Solid domains are initially created in a simulation box by arranging spherical

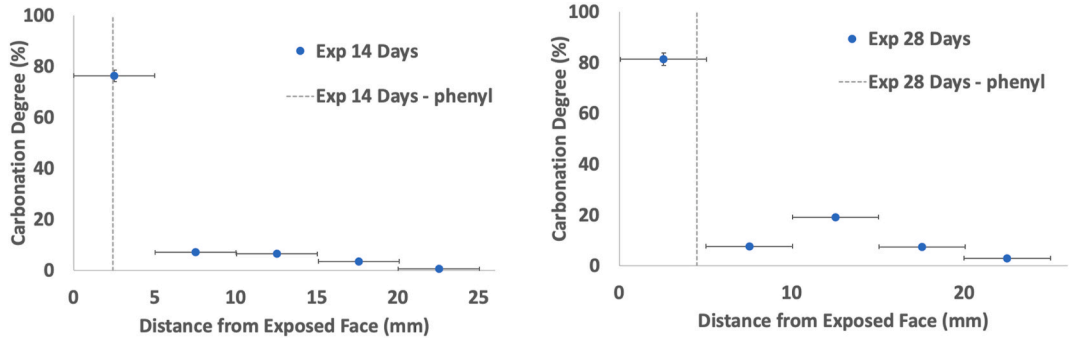

Fig. 2. Experimental results on carbonation degree and depth of penetration at 14 and 28 days [29] The dotted line shows the carbonation depth measured from phenolphthalein discoloration; the blue dots show the same quantity measured with more accurate thermogravimetric analysis. (For interpretation of the references to colour in this figure legend, the reader is referred to the Web version of this article.)

monodisperse particles of CH in a crystalline face centred cubic (FCC) lattice, and by filling part of the remaining space with spherical monodisperse particles of C-S-H in a disordered arrangement whose maximum density is dictated by the random close packing (RCP) limit: see Fig. 3. $CaCO_3$ particles form later during the simulation; they are also spherical and monodisperse and they spontaneously arrange to form both disordered and crystalline clusters. All particles interact via effective potentials (energy as a function of distance), e.g. the harmonic pair potential in Fig. 4, whose spatial derivatives provide the interaction forces. The features of the interaction potentials determine in which lattice arrangement the particles are mechanically stable; for the radial interactions and monodisperse spherical particles in this work, the densest mechanically stable lattices for the solids are FCC for CH and $CaCO_3$, and RCP for C-S-H (in this latter case, C-S-H cannot form a crystalline FCC lattice simply because it is forced into a disordered arrangement from the very beginning). Some space remains empty between the particles; this describes the pore structure of the paste, within which the implicit pore solution is modelled as average concentrations of multiple ionic species: $[Ca^{2+}]$, $[OH^-]$, $[CO_3^{2-}]$, $[H^+]$ and $[H_4SiO_4]$.

In this work, each solid particle represents only one molecule of the corresponding phase, which is the minimum possible coarse-graining above atomistic simulations; the advantage of this choice is that reaction rate equations can be obtained directly from Transition State Theory (TST) with a minimum number of assumptions. By contrast a coarser graining, with each particle representing thousands or millions of molecules, would require additional assumptions on nucleation and growth mechanisms (e.g. see Shvab et al. [33]) and this would reduce the predictive ability of the simulations. Minimum coarse-graining limits the length scale that can be modelled with these particles. For instance larger cracks in the order of micrometre cannot be simulated using these nanometre sized particles as the computations will be impractically costly. Other limitations that stem from the choice of minimum coarse-graining will be pointed out and discussed where relevant in the article. The simulations of particle dissolution and precipitation are performed using MASKE, a recently developed Kinetic Monte Carlo software [33].

The particles in the simulations interact via harmonic pair potentials as described in Coopamootoo & Masoero (2020) [34]. For two interacting particles of the same type, e.g. CH interacting with CH, the interaction energy U as a function of interparticle distance r is plotted in Fig. 4 and its expression is:

$$U(r) = \begin{cases} \frac{1}{2}\mathrm{k}(r - r_0)^2 - \varepsilon_0 & if\ r < r_c \\ 0 & if\ r \geq r_c \end{cases} \quad (1)$$

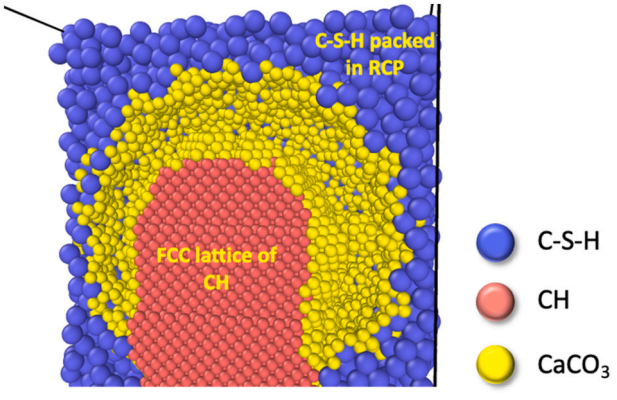

Fig. 3. Configuration of particle species during a typical simulation, CH in a face centred cubic FCC lattice, C-S-H in a disordered arrangement with maximum density dictated by the random close packing RCP limit, and $CaCO_3$ forming both FCC and RCP domains during its simulated precipitation.

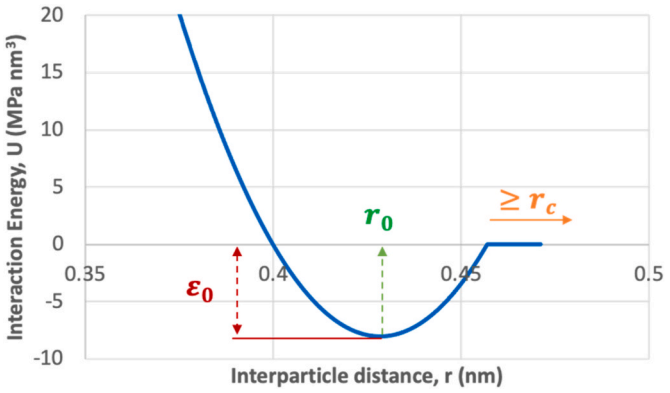

Fig. 4. The CH-CH harmonic pair potential showing the minimum energy at equilibrium (ε_0), equilibrium distance (r_0) and cut-off distance (r_c).

where $\mathrm{k} = EA/r_0$, E being Young's modulus of the solid in the particle and $A = \pi D^2/4$, where D is the diameter of the particle. Assuming that the molecules are spherical, D is calculated from the molar volume V_M of the phase that the particle represents, $D = \left(\frac{6V_M}{\pi N_A}\right)^{1/3}$, where N_A is the Avogadro number. The molar volumes of the three solids considered in this work are provided in Table 1; the molar volume of C-S-H includes the inter-layer pores but not the gel pores, since the latter are explicitly considered in the simulations as part of the remaining empty space between C-S-H particles: see Fig. 3. For the equilibrium distance between particles, r_0, one may be tempted to equate it to D, but that would leave artificial pores in-between particles even when they are arranged in their densest possible lattice: e.g. see CH in Fig. 3. Indeed, the intrinsic porosity of the FCC and RCP lattices in this work are respectively 26% and around 34%. To compensate for this artificial porosity, see Coopamootoo et al. [34] obtained an expression to reduce the interparticle distance to $r_0 = Df^{1/3}$. Here f is the packing fraction of the densest lattice (for FCC, f=0.74, RCP, f=0.64). This returns the correct molar volume of solid domains when the particles forming them are arranged in their densest possible configuration.

Still in Equation (1), ε_0 is the minimum energy at equilibrium.

$$\varepsilon_0 = \frac{\gamma\Omega}{n_{kink}} \quad (2)$$

where γ is the water-solid interfacial energy for the solid in the interacting particles; Ω is the surface area of the particle and n_{kink} is the average number of neighbors for a particle occupying a kink position in their densest lattice. For crystalline lattices, n_{kink} is simply half the number of neighbors of a particle in the bulk, e.g. 12/2 = 6 for FCC lattices. The cut-off distance, r_c is associated with the failure strain of the solids at the length-scale of the particle diameter, which is the nanometre here. At such length-scales, molecular simulations of typical crystalline cement minerals indicate an $\frac{r_c}{r_0}$ ratio that is usually around 1.05–1.10 [35]. The parameters used for the calculation of the interaction potentials between same-species particles are provided in Table 1. Later sections will extend Equation (1) to the case of interacting particles from different solids (e.g. CH with $CaCO_3$) and will explain how n_{kink} is determined for C-S-H in its non-crystalline, RCP arrangement.

Among the different polymorphs of $CaCO_3$ we assume that calcite, the most abundant and stable form, will be precipitated. For $CaCO_3$, we do not assign a lattice a priori and the interactions in Equation (1) will lead to the formation of both RCP and FCC domains. However, because of the ability of $CaCO_3$ to crystallise, we will assign lattice constants based on the FCC lattice for $CaCO_3$. The $CaCO_3$ -water interfacial energy provided is based on the surface energy of amorphous calcite. Experiments show that calcite formed at early stages may not be crystalline [36] (which has a high interfacial energy with water); instead,

Table 1
Parameters for the calculation of interaction potentials between same-species particles.

Solid Species	Molar Volume, V (cm^3/mol)	Particle Diameter, D (nm)	Young Modulus, E (GPa)	Packing fraction of solid lattice, f	Number of neighbors for a kink position, n_{kink}	Water-solid interfacial energy, γ (mJ/m^2)
$Ca(OH)_2$	32.81 [37]	0.47	48 [38]	0.74	6	68.4 [39]
C-S-H	110 [40]	0.81	63.6 [41]	0.64	4.44 (Section 2.1)	87.6 [42]
$CaCO_3$	36.90 [37]	0.49	69.9 [43]	0.74	6	32 [36]

nucleation and growth of calcite typically starts with an intermediate amorphous form of calcite with lower interfacial energy with water, which lowers the energy barrier to overcome initially. We use this lower energy to calibrate our potentials for $CaCO_3$.

The species that are considered in the implicit model of the pore solution are: Ca^{2+}, CO_3^{2-}, H_4SiO_4, H^+, OH^-, and H_2O. Table 2 shows the concentrations assigned to these species at the start of the simulation, as well as their charges. The initial concentration of H_4SiO_4 is taken from Jennings et al. [44], where aqueous solubility curves of C-S-H show that typical experimental values for silicate ion concentrations in solution range between 10^{-2} and 10^{-1} mmol/L. The concentration of OH^- is set to impose a pH of 12.5, which is typical for OPC-based concrete during its early stages of carbonation [45]. The presence of other alkali ions such as Na^+, K^+ etc., have an impact on buffering the pH of solution. However, in this work we are not presenting a realistic solution speciation model. Such a model would involve a free energy minimization for the solution, mass balance of ionic species. thus predicting the correct thermodynamics of the solution (example see Valentina et al., 2019 [46]). This is a direction which needs to be explored and a potential future implementation in MASKE. However, in this work a simplification is made by which the pH is fixed by fixing the OH^- ion concentration. This pH is considered to be the grant product of all the chemical speciation, and effect of alkalis and mass balance taking place in solution.

The initial concentration of CO_3^{2-} was calculated based on Henry's law which gives the concentration of CO_2 in water at equilibrium with the atmosphere. The concentrations of OH^-, H_4SiO_4 and CO_3^{2-} are fixed throughout the simulation run and only the concentration of Ca^{2+}, viz. $[Ca^{2+}]$, is allowed to vary. $[Ca^{2+}]$ is initially set to zero, which triggers a rapid dissolution of CH for the first few steps of the simulations, before it stabilizes around an equilibrium value once precipitation of $CaCO_3$ starts. Since $[H_4SiO_4]$ is fixed, in principle C-S-H could indefinitely form or dissolve during a simulation, but the results will show that this does not happen and the number of C-S-H particles in the system remain approximately constant while carbonation progresses, and CH is still present. This model of the solution is clearly simplified, in that numerous other ionic species may form even when just considering a calcium-silicate-carbonate solution [26]. However, the species modelled here are usually considered as the main ones contributing to the reactions underlying the carbonation of OPC pastes. Charge neutrality in the solution is ensured by tuning the concentration of H^+ ions, which effectively represents any positive ion in solution since none of the chemical reactions in this work involve H^+ directly.

The conversions between solids and solution are determined by chemical reactions; Table 3 collects those considered in this work, along with their key kinetic and thermodynamic parameters. More details on how these parameters appear in the reaction rate equations will follow later in this section.

Table 2
Initial composition of the pore solution in the simulations. a_i and b_i are parameters that will be introduced and used later for the calculation of activity coefficients.

Species in solution	Initial concentrations (mmol/L)	Charge (z_i)	a_i (nm) [47]	b_i [47]
Ca^{2+}	0	2	0.486	0.150
H_4SiO_4	0.1	0	0.000	0.000
OH^-	30	−1	1.065	0.064
CO_3^{2-}	0.01132	−2	0.540	0.064
H^+	30.02264	1	0.900	0.000

Table 3
Chemical reactions considered in the simulations, along with their corresponding equilibrium constants K_{eq} and activation free energies $\Delta G^{\ddagger}_{diss/prec}$.

Reaction (dissolution)	$K_{eq,d}$	$\Delta G^{\ddagger}_{diss}$
$Ca(OH)_2 \rightarrow Ca^{2+} + 2\ OH^-$	6.30866×10^{-6} [47]	122.85 [48]
C-S-H $\rightarrow 2\ Ca^{2+} + H_4SiO_4 + 4$ OH-	1×10^{-17} [49]	145.121 [42]
$CaCO_3 \rightarrow Ca^{2+} + CO_3^{2-}$	3.31157×10^{-9} [47]	119.41525 [50]
Reaction (precipitation)	$K_{eq,p} = \frac{1}{K_{eq,d}}$	$\Delta G^{\ddagger}_{prec}$
$Ca^{2+} + 2\ OH^- \rightarrow Ca(OH)_2$	1.58512×10^{5} [47]	74.052 [48]
$2\ Ca^{2+} + H_4SiO_4 + 4$ OH- $\rightarrow$ C-S-H	1×10^{17} [49]	−44.4 [42]
$Ca^{2+} + CO_3^{2-} \rightarrow CaCO_3$	3.02×10^{8}[47]	39.064 [50]

The MASKE software employs the following expressions for the unimolecular rates of particle dissolution and precipitation (as shown in Fig. 5):

$$r_{diss} = \frac{k_B T}{h} \frac{c^{\ddagger}}{\gamma^{\ddagger}} \exp\left[-\frac{\Delta G^{\ddagger}_{diss}}{k_B T}\right] \exp\left[\frac{-\Delta U_{diss} - U_{kink}}{k_B T}\right] Q_{r,d} V_t^{\alpha/3} \quad (3)$$

$$r_{prec} = \frac{k_B T}{h} \frac{c^{\ddagger}}{\gamma^{\ddagger}} \exp\left[-\frac{\Delta G^{\ddagger}_{prec}}{k_B T}\right] Q_{r,p} \Delta V . V_t^{\alpha/3} \quad (4)$$

k_B is the Boltzmann constant, T is the temperature, h is the Planck constant, $\gamma^{\ddagger}$ and $c^{\ddagger}$ are the activity coefficient and standard state concentration of the activated complex. Reaction rates for dissolution and precipitation are typically expressed in number of reactions per unit area and per unit time, in which case $c^{\ddagger}$ is in number of activated complexes per unit area as well. ΔV is a user-defined small volume (usually in the order of D^3) by which the simulation box is discretized when sampling possible positions for the precipitation of new particles: see Shvab et al. [33]. V_t is the tributary volume of a particle, which is the volume of the attractive interaction basin within which a particle would attract towards itself another neighbor particle; one can take $V_t \sim D^2\ r_c$ for a particle being part of the surface of a larger crystal. $\Delta G^{\ddagger}$ is the standard state activation energy, $\Delta G^{\ddagger}_{diss}$ for dissolution and $\Delta G^{\ddagger}_{prec}$ for precipitation. $Q_{r,p}$ and $Q_{p,p}$ are the activity products of the reactant and product molecules of a precipitation reaction; $Q_{r,d}$ and $Q_{p,d}$ are the analogues for a dissolution reaction. In all the reactions considered here, listed in Table 3, the reactants in dissolution reactions are only solid molecules, as well as the products in precipitation reactions, hence $Q_{r,d} = Q_{p,p} = 1$ (because stress-free solids are conventionally taken as being in the standard state). ΔU_{diss} is the change in interaction energy following the dissolution of a particle, and U_{kink} is the interaction energy between a kink particle and its nearest neighbors. α is the spatial dimensionality of $c^{\ddagger}$, with $\alpha = 3$ if $c^{\ddagger}$ is per unit volume and $\alpha = 2$ if $c^{\ddagger}$ is per unit surface area. The derivation and physical meaning of these equations and their validation are discussed in earlier works [33,34].

The straight rate Equations (3) and (4) can be combined to express net rates of particle dissolution and precipitation:

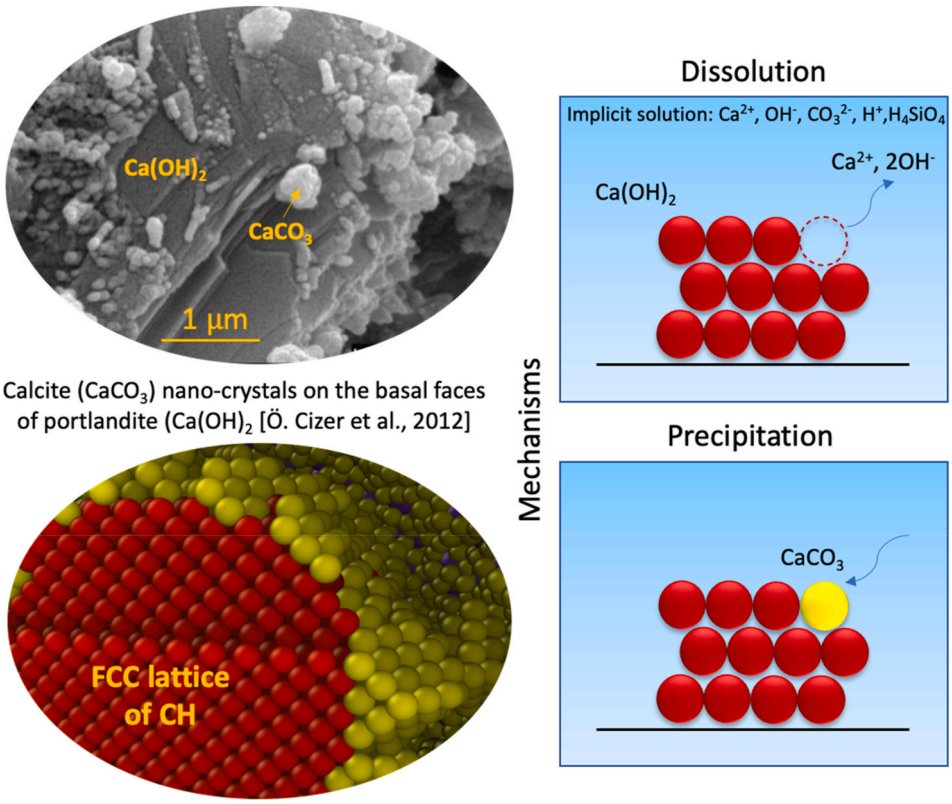

Fig. 5. Dissolution of $Ca(OH)_2$ and precipitation of $CaCO_3$ from the implicit solution. Calcite growth over CH, as observed from SEM images [51] is compared to calcite growth from the simulations.

$$r_{diss} = r_d - r_{d-} = \frac{k_B T}{h}\frac{c^{\ddagger}}{\gamma^{\ddagger}} \exp\left[-\frac{\Delta G^{\ddagger}_{diss}}{k_B T}\right]\left(\exp\left[\frac{-\Delta U_{diss} - U_{kink}}{k_B T}\right] Q_{r,d} - \frac{Q_{p,d}}{K_{eq,d}}\right) V_t^{\alpha/3} \quad (5)$$

$$r_{prec} = r_p - r_{p-} = \frac{k_B T}{h}\frac{c^{\ddagger}}{\gamma^{\ddagger}} \exp\left[-\frac{\Delta G^{\ddagger}_{prec}}{k_B T}\right]\left(Q_{r,p} - \exp\left[\frac{-\Delta U_{diss} - U_{kink}}{k_B T}\right] \frac{Q_{p,p}}{K_{eq,p}}\right) \Delta V . V_t^{\frac{\alpha}{3}} \quad (6)$$

r_{d-} and r_{p-} are the backward rates of dissolution and precipitation which are analogous to r_{diss} and r_{prec} respectively in Equations (3) and (4). Simulations using net rates, instead of straight ones, are less computationally expensive because they avoid resolving all fluctuations between individual events of particle dissolution cancelling previous events of particle precipitation and vice versa, focussing instead only on the averaged net difference between such events. However, for some phenomena, such fluctuations can be very important, e.g. to simulate the formation and evolution of pre-nucleation clusters (see Shvab et al. [33] for more discussion). This work will mainly adopt net rates, but some comparisons with simulations using straight rates will be provided too in the results.

Equation (5) can be rearranged to recover the usual form of dissolution rates from Transition State Theory (TST), viz. $r^{TST}_{diss} = k_{diss}(1-\beta)$. In doing so, the expression for the rate constant becomes $k_{diss} = \frac{k_B T}{h}\frac{c^{\ddagger}}{\gamma^{\ddagger}} \exp\left[-\frac{\Delta G^{\ddagger}_{diss}}{k_B T}\right]$. The exponential term $\exp\left[\frac{-\Delta U_{diss} - U_{kink}}{k_B T}\right]$ is equal to 1 for kink particles, and indeed an underlying assumption of TST is that all surface particles are treated as if they are occupying a kink position (see more discussion in Coopamooto et al. [34]). For the reactions considered here, $Q_{r,d} = 1$ as already mentioned, and the saturation index β of the solid finds its usual definition as $\beta = \frac{Q_{p,d}}{K_{eq,d}}$. The last term in Equation (5), $V_t^{\alpha/3}$, is proportional to the surface area of a particle and returns the usual normalization of the TST rates, which is indeed per unit area, i.e. $r^{TST}_{diss} = r_{diss}/V_t^{\alpha/3}$. Following similar steps, also Equation (6) can be reduced to the form $r^{TST}_{prec} = k_{diss}(\beta - 1)$ where $\beta = \frac{Q_{r,p}}{K_{eq,d}}$ (note that $Q_{r,p} = Q_{p,d}$, hence β here is exactly the same as for the TST version of the dissolution equation above; also note that the rate constant for precipitation is correctly the same one as for dissolution). The saturation index β of a solid species determines whether a particle will dissolve or precipitate, with equilibrium at $\beta = 1$, dissolution being favoured when $\beta < 1$, and $\beta > 1$ favouring precipitation.

The constants used in Equations (3)–(6), $\Delta G^{\ddagger}$ and K_{eq} are provided in Table 3. The activity product depends on the chemical reaction that is being considered and is calculated as:

$$Q_{r,p} = \prod_{i=1}^{n_r} \gamma_i c_i \quad (7)$$

where n_r is the number of molecules involved in the reaction and c_i is the concentration of the ith molecule involved in the reaction, whose activity coefficient γ_i is computed using the Debye Huckel Theory as:

$$log_{10}(\gamma_i) = \frac{-z_i^2 A\sqrt{I}}{1 + Ba_i\sqrt{I}} + b_i\sqrt{I} \quad (8)$$

A and B are solvent-specific constants which are equal to 0.51 and 3.29 nm^{-1} for water, a_i is the hydrated radius of the molecule and b_i is a molecule-specific constant as given in Table 2. The ionic strength (I) of the solution is computed as:

$$I = \sum_{i=1}^{n_s} c_i z_i^2 \quad (9)$$

where n_s is the number of molecular species in solution, c_i is the

concentration of the ith ionic species, and z_i its charge as provided in Table 2.

2.1. Parameterising amorphous C-S-H for solubility

The previous section mentioned that, for particles in a crystalline lattice such as CH, $n_{kink} = n_{bulk}/2$. For amorphous particles such as C-S-H, the densest arrangement imposed in the simulations here is RCP, which one could also use to compute an average value for n_{bulk}, and thus of n_{kink} which in turn informs ε_0 in Equation (2) and its contribution to ΔU_{diss} and the rates. However, working with an average value of n_{bulk} from a random arrangement would not return a system that is at equilibrium when $\beta = 1$ for two reasons: (i) particles on the surface of an RCP solid domain with approximately n_{kink} neighbors will actually feature a range of number of neighbors including and around $n_{bulk}/2$, hence some particle and surface sites will still support dissolution or precipitation also at $\beta = 1$; (ii) all particles in an RCP are under a self-equilibrated and spatially heterogeneous state of local stress (see Fig. 6(a)) which affects $\exp\left[\frac{-\Delta U_{diss} - U_{kink}}{k_B T}\right]$ in the rate equations, meaning that also for particles with approximately $n_{bulk}/2$ neighbors, the rate is not controlled solely by $(\beta - 1)$.

To overcome these two issues we adopted a trial and error method to determine an equivalent n_{kink} for the amorphous C-S-H system, which would give equilibrium at $\beta = 1$ when used to parametrize the interaction energy scale ε_0 in Equation (2) The method is based on the observation in Ref. [43] that the solubility of a spherical domain of particles arranged in a crystalline lattice is indeed controlled by kink particles [52], leading to equilibrium when $\beta = 1$. We generalise the same approach and create a spherical domain of particles, as shown in Fig. 6 (a), carving it out from a box that was previously filled with C-S-H particles at RCP using the random space-filling algorithm in Masoero & Di Luzio 2020 [41]. The carved domain is let to relax by energy minimization, to zero the average pressure in the domain. We then tune the equivalent n_{kink} in the expression of ε_0 until we get dissolution for $\beta < 1$, no dissolution for $\beta > 1$, and equilibrium at $\beta = 1$. The equivalent n_{kink} for C-S-H resulting from this approach was determined to be 4.44, which returns the dissolution curves in Fig. 6(b), which satisfy indeed equilibrium when $\beta \approx 1$.

2.2. Parameterising interaction potentials between dissimilar particles

Equation (1) is the interaction potential between pairs of particles from the same solid phase. For two particles representing different phases, 1 and 2, such as C-S-H and CH, Equation (1) can be re-written as:

$$U_{12}(r) = \begin{cases} \frac{1}{2}k_{12}(r - r_{12})^2 - \varepsilon_{12} & \text{if } r < r_{c,12} \\ 0 & \text{if } r \geq r_{c,12} \end{cases} \quad (10)$$

where k_{12} is the effective stiffness of the spring between 2 particles of different size and different Young's modulus. k_{12} is calculated as the harmonic average of $k_1 = E_1 A_1 / r_1$ and $k_2 = E_2 A_2 / r_2$, where r_1 and r_2 are the equilibrium distances for the two particles of each species when they are interacting with particles of their same type (cf. r_0 in Equation (1)); this gives $k_{12} = \frac{k_1 k_2}{k_1 + k_2}$. The equilibrium distance between the two particles of different species is is $r_{12} = \frac{r_1 + r_2}{2}$ and similarly the cut-off distance $r_{c,12}$ is the average of the individual cut-offs. ε_{12}, the minimum interaction energy between two particles of different species, is determined by modifying Equation (2) for ε_0, where γ was the water-solid interfacial energy when the two interacting particles were of the same species. Now, for two particles representing dissimilar phases, 1 and 2, such as C-S-H and CH, γ needs to be replaced by a term accounting for both the interfacial energy in particle 1 at contact with particle 2, γ_{12}, and the interfacial energy in particle 2 at contact with particle 1, γ_{21}. These values of interfacial energies are typically unknown from experiments; atomistic simulations could help estimate them, but the result of such simulations would likely entail large uncertainties. Hereafter, therefore, we derive an expression for ε_{12} by assuming that γ_{12} and γ_{21} are fractions of the respective water-solid interfacial energies, i.e. $\gamma_{12} = \gamma_1(1 - \kappa_{12})$ and $\gamma_{21} = \gamma_2(1 - \kappa_{21})$, with scalar parameters κ between 0 and 1, where 0 means that the interface with the other solid brings no energetic advantage compared to having a free surface in contact with water.

To express ε_{12} from these premises, consider the scenario in Fig. 7, where a large particle of species 1, with surface area A_1, is fully surrounded by smaller particles of species 2, with surface area A_2. Fig. 7 is in 2D for clarity, but the derivation below is for the 3D case. Now assume that particle 1 dissolves, leaving a hole (i.e., a water-particle 2 interface) with surface area A_1 where there was previously an interface between particles of type 2 and particle 1. From a macroscopic perspective, the change in system energy ΔU can be expressed exclusively in terms of interfacial energies (assuming stress-free conditions): $\Delta U(macro) = \gamma_2 A_1 - \gamma_{12} A_1 - \gamma_{21} A_1$. In the microscale MASKE simulations, instead, the same dissolution event would cause a change in energy that is due both to the surface energy of particle 1 (embedded in the U_{kink} term in Equation (3)) and the interaction energy between particle 1 and its n_{12} neighbors of type 2: $\Delta U(micro) = -\gamma_1 A_1 + n_{12}\varepsilon_{12}$. By equating ΔU_{diss}(macro) with ΔU_{diss}(micro) and remembering the definition above for the parameters κ we obtain:

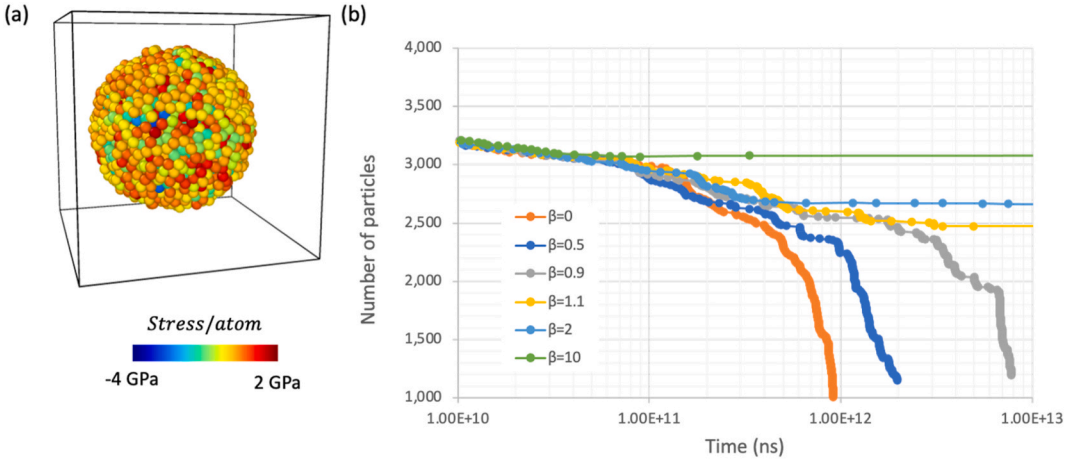

Fig. 6. (a) Spherical domain carved from an RCP arrangement of C-S-H particles. The colours of the particles highlight the heterogeneous distributions of stress which makes equilibrium not directly relatable to a purely topological quantity such as the number of neighbor particles. (b) Zero-rate dissolution-precipitation parametrization for C-S-H. (For interpretation of the references to colour in this figure legend, the reader is referred to the Web version of this article.)

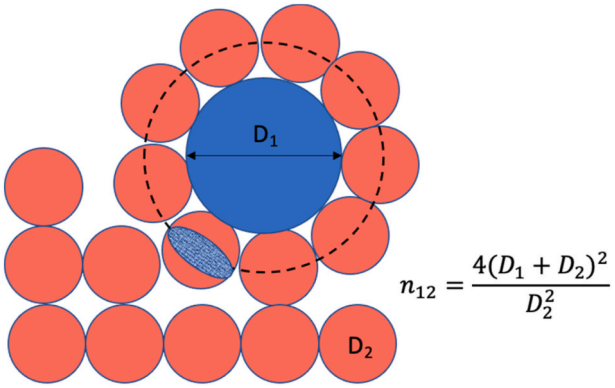

Fig. 7. Interactions and interfaces between particles of dissimilar types and sizes, and geometric expression for the number of neighbors n_{12}.

$$\varepsilon_{12} = \varepsilon_{21} = (\kappa_{12}\gamma_1 + \kappa_{21}\gamma_2)\frac{A_1}{n_{12}} \tag{11}$$

We set $\varepsilon_{12} = \varepsilon_{21}$ because we expect the interaction potential between particles of types 1 and 2 to be symmetric. Not knowing the exact values of κ, in this work our first attempt is with $\kappa_{12} = \kappa_{21} = 0.5$. The impact of assuming other values of κ on microstructure development and mechanical properties will be explored later in Section 3.5.

The last term to be quantified in Equation (11) is the number of neighbors n_{12} when particle 1 is fully surrounded by particles of type 2. A purely geometric estimate is shown in Fig. 7, where n_{12} is obtained by dividing the surface area of the dashed sphere, centred onto particle 1 and with diameter D_1+D_2, by the cross-sectional area of a particle of type 2 (i.e. πD_2^2). This expression is accurate when there is a large size difference between the particles, but it overpredicts the number of neighbors for an FCC lattice with similar-sized particles (i.e., if $D_1 = D_2$); for such FCC lattice, indeed, the correct number of neighbors would be 12, whereas the equation in Fig. 7 would predict $n_{12} = 16$. Since the particles in this work will have a quite similar size, we thus apply a correction factor of 12/16 obtaining $n_{12} = \frac{3(D_1+D_2)^2}{D_2^2}$.

2.3. The initial configuration

The initial configuration was created by the following steps. Starting from an initially empty simulation box, a CH crystal was created by arranging CH particles in an FCC lattice, filling 28% of the box volume (f_{CH}). This is the theoretical volume fraction of CH in a paste obtained from fully hydrating C_3S, forming C-S-H gel and CH [40]. The CH crystal was pre-dissolved for a few steps to create some imperfections on the surface from where dissolution can progress also when $\beta_{CH} \approx 1$ (Fig. 8 (a)). The porosity (η) for the C-S-H gel was taken as 34.5% [40], the amount computed for so-called 'low density' C-S-H in Jenning's colloidal model [53,54]. From this, the volume occupied by C-S-H particles (f_{C-S-H}) was calculated as 47% using the relation $f_{C-S-H} = (100 - f_{CH}) \times \eta$. Then C-S-H particles were added at random locations using the algorithm in Masoero and Di Luzio [41] whereby the insertion of 1000 particles is attempted at each packing step but then overlaps with existing particles are removed. When the target volume fraction of solid C-S-H (47%) is reached, the remaining 25% of empty space in the simulation box represents the gel porosity, as shown in Fig. 8(c).

A large cavity of size 6.322 nm (corresponding to ~10% of total volume fraction) was then carved out from the C-S-H at the center of the box, leaving the CH intact. The system was then relaxed by changing the box size until reaching zero average axial stresses in all directions using conjugate gradient energy minimization method. A seed of $CaCO_3$ is placed within the cavity (Fig. 8(d)). This larger void was created, and the calcite seed placed to provide space and a convenient location for $CaCO_3$ particles to cluster and grow into an extended crystalline domain, should

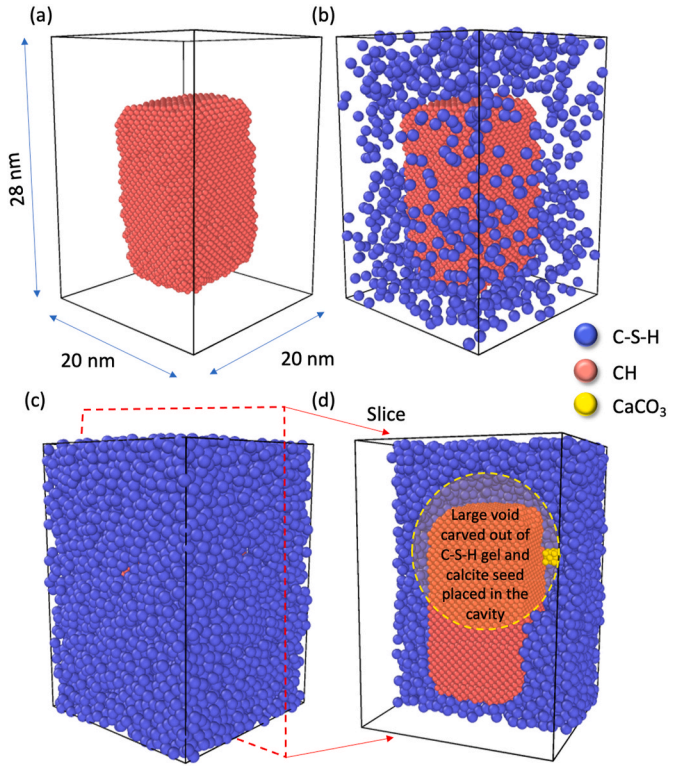

Fig. 8. (a) Pre-dissolved CH with imperfections, occupying a volume fraction of 28% of box, (b) C-S-H particles early during the C-S-H packing process and (c) after reaching a volume fraction of 47% of the box, leaving a gel porosity of 25%. (d) Large pore carved out, with a $CaCO_3$ seed placed in it.

the system kinetics favor such an outcome. The volume fraction of the larger void is in line with typical capillary porosity in cement paste. However, we do not call this a capillary pore because of its small size (<10 nm). Nevertheless, there is a clear difference in size between this larger cavity (6.322 nm) and to the smaller pores between C-S-H particles in his model, whose typical size in the order of a C-S-H particle diameter, i.e. 0.81 nm.

The dissolution-precipitation reactions were carried out using the simulation box in Fig. 8(d). The chemical evolution of the solution and the microstructural evolution of the solid were monitored and they will be presented and analysed in Section 3.2. The effective reaction rate constants determined from these simulations were then applied to a reactive chemical transport model as detailed in the next section.

2.4. Reactive chemical species transport

In the present work, the effective reaction rate constants determined from the above simulations were then applied to a reactive chemical transport model to simulate a carbonation problem at the macroscale. The carbonation of cementitious materials is characterised by the diffusion of carbon dioxide from the environment into the specimen through the pore network, its subsequent dissolution into the moisture phase, and the reaction of the dissolved carbon with calcium ions (produced through the dissolution of mineral phases), to form calcium carbonate.

To simulate the carbonation problem, we employed the 2D reactive transport finite element model presented in Freeman et al., 2019 [28]. In the example problem considered, see Fig. 9, the saturation degree of the sample with pore water is uniform at 0.2928 and as such, moisture transport does not take place, though it is included in the model; only diffusion of CO_2 and Ca^{2+} therefore take place. In addition, we assume that both changes in porosity (and therefore diffusion coefficients) and

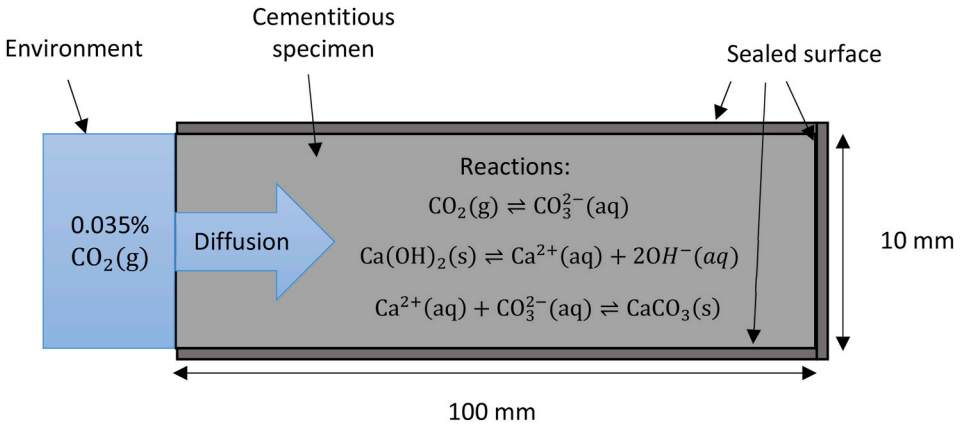

Fig. 9. Schematic of reactive transport of carbonation problem.

solution volume due to the reactive transport are negligible. The chemical species considered were $CO_2(g)$, $CO_3^{2-}(aq)$ and $Ca^{2+}(aq)$. The reactive solid species considered were $Ca(OH)_2(s)$ and $CaCO_3(s)$, whilst the remaining solid volume was assumed inert. In this work, the chemical species and reactive solid species were considered in terms of concentrations (mol/L). The initial concentration of $Ca(OH)_2(s)$ was calculated from the percentage by weight given in the experimental data, whilst the initial concentration of $CaCO_3(s)$, was assumed to be zero (see Section 3.3).

2.4.1. Transport of chemical species

The transport of species is governed by the mass balance equation that reads:

$$\frac{\partial\left(nS_j c_i^j\right)}{\partial t} + \nabla \bullet \left(- nS_j D_i^{mol} \nabla c_i^j\right) + f_i^j = 0. \tag{12}$$

where $j = g \vee l$ indicates a gaseous or aqueous species respectively, n is the porosity, S_j is the degree of saturation of the pores (with gas or liquid), c_i^j denotes the concentration of species, i, D_i^{mol} is the molecular diffusivity of species, i, and $f_i^j = nS_j r$ is the sink/source term arising from dissolution/precipitation reactions, where r is the reaction rate.

In the present work, we consider the transport of $CO_2(g)$ and $Ca^{2+}(aq)$, governed by Equation (11), whilst the $CO_3^{2-}(aq)$ content is determined through a local equilibrium condition (see next section). It is noted that the diffusion of $CO_3^{2-}(aq)$ is not considered as it is much slower than the rate of transport of $CO_2(g)$ and the dissolution reaction ($CO_2(g) \rightleftharpoons CO_3^{2-}(aq)$).As such, transport of $CO_3^{2-}(aq)$ into the sample is governed by the diffusion and dissolution of $CO_2(g)$.

2.4.2. Chemical reactions

The chemical reactions considered are the dissolution of $CO_2(g)$ into the liquid phase, and the precipitation/dissolution of $Ca(OH)_2(s)$ and $CaCO_3(s)$. The dissolution of $CO_2(g)$ is assumed to be sufficiently fast such that a local equilibrium exists given as (where K_H is Henry's constant):

$$CO_3^{2-}(aq) = K_H CO_2(g) \tag{13}$$

It is assumed that all dissolved carbon is in the form of $CO_3^{2-}(aq)$ ions. This is a valid assumption at the high pH typically associated with cementitious materials, but may not be as the pH drops with carbonation. In such cases, a simple correction could be employed based on a Bjerrum plot (Turley et al., 2004) [55].

The dissolution/precipitation of $Ca(OH)_2(s)$ and $CaCO_3(s)$ are governed by the following rate equations, where the kinetic rate constants k will later be calibrated from the results of the MASKE simulation:

$$r_{Ca(OH)2} = k_{Ca(OH)2}\left(1 - \beta_{Ca(OH)2}\right)S_l^{3.7} \tag{14}$$

$$r_{CaCO3} = -k_{CaCO3}\left(1 - \beta_{CaCO3}\right)S_l^{3.7} \tag{15}$$

where the effect of pore saturation degree on the reaction rate has been accounted for [56].

An important consideration is the effect of the chemical reactions on the pH of the pore solution, which is important for a range of issues, including reinforcing bar corrosion [57]. The pH depends upon the concentration and interaction of ions in the pore solution. In the present work, such interactions are not accounted for and the pH is kept constant during the simulations. An indication of the possible pH change can be estimated from the degree of carbonation of the sample according to the results of Chang and Chen, 2006 [58]:

$$pH = \begin{cases} 12.5, \forall D_{carb} \le 1 \\ a_1 + a_2\ tanh^{-1}\left(1 - \dfrac{D_{carb}}{a_3}\right), \forall D_{carb} \ge 1 \bigwedge D_{carb} \le 90 \\ 7.5, \forall D_{carb} \ge 90 \end{cases} \tag{16}$$

where $a_1 = 9.157$, $a_2 = 1.329$, $a_3 = 50$ and D_{carb} is the degree of carbonation given as:

$$D_{carb} = 100 * \left(\frac{CaCO_3(s)}{CaCO_3^{max}(s)}\right) \tag{17}$$

in which the *max* superscript indicates the value at complete carbonation (i.e. when all of the locally available CH has been carbonated).

2.5. Boundary nucleation and growth

The boundary nucleation and growth (BNG) model is a heterogenous version of the classical Avrami nucleation and growth model. The key difference is that nuclei appear only on surfaces and crystals grow as hemispheres from these surfaces (Masoero, 2018) [59]. The extended area fraction (Y^e) of all spherical crystals nucleated on a crack face at time $t = 0$ and at a distance y from the boundary is given as:

$$Y^e = N_s \pi \left\{ \left(G_0 * \xi(t)\right)^2 - y^2 \right\} \tag{18}$$

where {} are Macaulay brackets, N_s are the number of nuclei per unit surface area, t is the time and $\xi(t)$ is an effective time defined such that (Bullard et al., 2015) [60]:

$$\int_0^t G(t)dt = G_0 * \xi(t) \tag{19}$$

where $G(t)$ is the crystal growth rate given as:

$$G(t) = G_0(\beta_{CaCO3}(t) - 1) \tag{20}$$

in which G_0 is a linear growth rate constant.

From probabilistic considerations, the true area fraction (i.e. the area fraction once overlapping regions are removed), is equal to the probability that a randomly chosen point, c, belongs to the transformed (crystallised) phase. If we let X be the distance from c to the nearest nucleus, assuming that nucleation sites are randomly distributed on the crack face, this is equivalent to:

$$P\{X \le r\} = Y = 1 - exp(-Y^e) \tag{21}$$

where r is the radius of the crystals.

In the above, the area related to overlapping crystals in the tangential direction to the crack faces has already been removed, but the areas related to overlapping crystals in the normal direction to the crack faces has not. For crystal growth from two crack faces, at some point the crystals will begin to overlap in the centre of the crack. The next step is to find the true volume fraction, following the removal of these regions of overlap. The true volume fraction considers areas of transformed phase from each crack face, and disregards areas that overlap. This is accounted for using probabilistic arguments. At a given point within the crack the true area fraction is given as:

$$\begin{aligned} Y^p &= P\{X_r \le x_r\} \vee P\{X_l \le x_l\} - P\{X_r \le x_r\} \\ &\wedge P\{X_l \le x_l\} = \left[1 - exp\left(-Y_r^e\right)\right] + \left[1 - exp\left(-Y_l^e\right)\right] - \left[1 - exp\left(-Y_r^e\right)\right] \\ &* \left[1 - exp\left(-Y_l^e\right)\right] \end{aligned} \tag{22}$$

where Y^p represents the area fraction at a given point in the crack and the l and r subscripts indicate the left and right crack faces respectively. In the above, it is implicitly assumed that the random spatial distribution of nuclei on each crack face is independent of the other. To get the volume fraction, Z, this term needs to be integrated across the crack width, wc:

$$\begin{aligned} Z = O_v^b \int_0^{wc} &\left[\left[1 - exp\left(-Y_r^e(wc - y)\right)\right] + \left[1 - exp\left(-Y_l^e(y)\right)\right] - \left[1 - exp\left(\right.\right.\right. \\ &\left.\left.\left. - Y_r^e(wc - y)\right)\right] * \left[1 - exp\left(-Y_l^e(y)\right)\right]\right] dy \end{aligned} \tag{23}$$

where O_v^b is the crack face area per unit volume.

Note that in the above, the dependencies of the area fractions on the distance from the crack face have been included to show that for the left crack face distance is measured from left to right and for the right crack face vice versa.

The flowchart in Fig. 10 summarises the overall methodology and the communication of parameters across length scales described in methodology. The relevant equations, tables and results in the manuscript are referred to in the flowchart.

3. Results and discussion

In the following sections we first examine the relative effect of using net rates vs straight rates and find that both give comparable results, although the simulations with net rates are approximately 2.5 times faster. Following this we use net rates to run the MASKE simulation on the initial configuration described in Section 2.3; we examine two emerging regimes, one of $CaCO_3$ covering preexisting domains of CH and C-S-H, and the other regime of $CaCO_3$ particles assembling to form growing crystals. In both cases we quantify solution properties such as concentration of ions and saturation indices of solids. We then fit the reaction rates from the growth regime to the standard rate Equations (14) and (15) above, thus computing values for the effective rate constants in said equations. These constants are subsequently supplied to the macroscale reactive transport model, obtaining results on carbonation depths to compare to the experimental results in Fig. 2.

3.1. Dissolution-precipitation using net and straight rates

Three reaction mechanisms govern the carbonation in the model cement paste considered here: dissolution of CH and C-S-H, raise in the

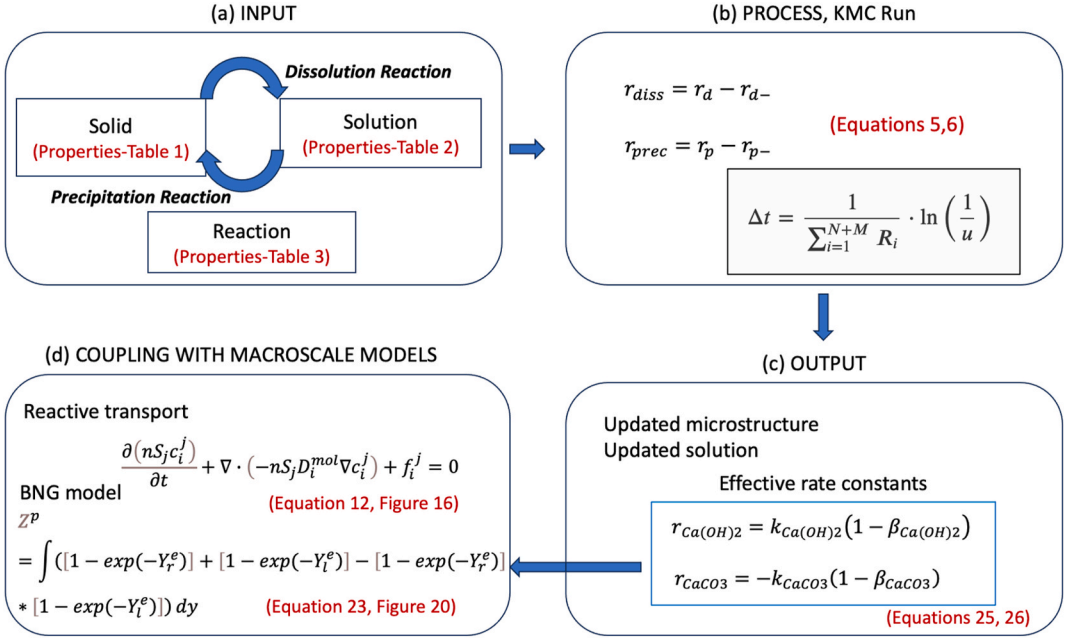

Fig. 10. Flowchart depicting the overall methodology and communication of parameters across length scales. (a) The input parameters for solid, solution and the reaction which is the conversion between solid and solution are provided to MASKE (b) MASKE performs the KMC run according to the molecular rate equations defined. (c) The updated microstructure and solution properties during the run are used to determine the effective rate constants (d) The effective rate constants are supplied to the higher scale models and comparison with experimental results are obtained.

concentration of Ca^{2+} ions in solution, and subsequent precipitation of $CaCO_3$. When adopting the straight rates in Equations (3) and (4), however, also the reverse reactions must be modelled, especially in near-equilibrium conditions, i.e. CH and C-S-H precipitation and $CaCO_3$ dissolution, as shown in Table 3. When adopting net rates instead (Equations (5) and (6)), one can limit the allowed mechanisms to only CH and C-S-H dissolution, and $CaCO_3$ precipitation. Therefore, a test run on a small simulation box (10x10 × 14 nm) was performed to compare whether more-efficient simulations, using net rate equations, would yield comparable results as more accurate simulations using straight rates.

Fig. 11 shows the number of particles of CH, C-S-H and $CaCO_3$ during the test runs. CH dissolves, $CaCO_3$ precipitates and C-S-H remains essentially constant. Note that $[H_4SiO_4]$ is fixed, so C-S-H could potentially grow or dissolve indefinitely thus contributing significantly to the amount of Ca^{2+} in solution. However, the simulation predicts the realistic result whereby C-S-H kinetics does indeed contribute negligibly to early carbonation, with only a few C-S-H particles dissolving and reprecipitation in isolated regions with particularly low connectivity with the rest of the C-S-H amorphous domain. Hence, $CaCO_3$ precipitation is tightly linked to the dissolution of CH, since only the latter provides a continuous supply of Ca^{2+} ions throughout the simulation. The results show that both net and straight rates give similar results; however, the simulation using net rates in Fig. 6(b) was ~2.5 times faster than that using straight rates in Fig. 6(a), hence net rates will be used for the larger simulations in the following sections.

3.2. $CaCO_3$ precipitation into a larger pore

Full simulations of carbonation were run on the larger simulation box (20x20 × 28 nm), with initial configuration featuring crystalline CH, amorphous C-S-H and a relatively large void providing space for $CaCO_3$ particles to cluster and form larger solid domain, mimicking what happens in the capillary pores and cracks of concrete: see Fig. 12. Precipitation of $CaCO_3$ would normally favor any tiny pores within the C-S-H gel phase, because that would reduce the internal water-solid interfacial energy of the C-S-H gel itself. Such a process of intra-gel precipitation, however, is not very impactful in real carbonation of concrete, because limited by slow ion diffusion into the C-S-H gel. The simulations overestimate this process because they implicitly assume instantaneous diffusion by considering a uniform distribution of ion concentrations everywhere in the simulation box. Therefore, to favor a more realistic formation of extended $CaCO_3$ domains in larger pores, precipitation of $CaCO_3$ particles has been allowed only within the larger spherical void plus the first couple of layers of C-S-H gel on the pore surface.

The initial configuration in Fig. 12 (a) also includes a small seed of solid $CaCO_3$ in the larger spherical void; this is done to investigate whether and to what an extent the precipitation of new $CaCO_3$ particles would benefit from or rely on such a favorable site; it will turn out however that the impact of this seed on the overall kinetics and morphology is very limited.

Fig. 13 shows the precipitation curve for $CaCO_3$ obtained here, which follows a qualitatively similar trend as for the preliminary simulations on a smaller box presented in Section 3.1. The curve in Fig. 13 displays two distinct regimes: (1) Coverage, during which the $CaCO_3$ particles form a single layer covering the existing interfaces between the large spherical void and the surfaces of the C-S-H gel and CH domains; (2) Growth, during which $CaCO_3$ organizes into crystalline domains that grow three-dimensionally into the volume of the spherical void. The inset in Fig. 13 shows the concentration of Ca ions in solution during both the coverage and growth regimes; the faster precipitation rate during coverage is consistent with the concentration of Ca ions being smaller during this regime, 1-2 mmol/L against 6-7 mmol/L during the slower, subsequent regime of growth. Throughout the simulation, the concentration of Ca ions remains correctly below the equilibrium value of approx. 20 mmol/L for CH dissolution, at the pH of 12.5 imposed here.

Coverage is fast and dominates the first part of the simulation here. Growth is initially slower because it requires a sufficiently large solid cluster to form before it can significantly impact the rates. The initial prevalence of coverage therefore is likely a product of the small-scale simulation and minimal coarse graining employed here, which means that full coverage is reached before larger crystalline clusters can grow enough to take over the rate. At the larger scale of micrometre-sized crystals, some coverage may still take place initially but, after some time, the growth process of larger $CaCO_3$ crystals will become the main contributor to the rate, as evidenced in experimental SEM images showing large crystals of calcite forming in carbonated pastes (e.g., in Fig. 1 and in Fig. 5). Furthermore, the importance of the coverage regime in the simulations relies on the interfacial energies between C-S-H and $CaCO_3$ and between CH and $CaCO_3$, which impact the ΔU_{diss} term in the net rate equation. In this work the solid-solid interfacial energies are established through a rather arbitrary choice of the κ_{12} factors, as discussed in Section 2.2, therefore the impact of different values of such interfacial energies on the coverage and growth regimes will be investigated later in Section 3.5. By contrast, the value of the $CaCO_3$-water interfacial energy is better known, and it controls growth. Therefore, putting together the artifact of the length scale favouring coverage, over growth, the uncertainty on the $CaCO_3$-CSH and CH-$CaCO_3$ interfacial energies, and the likelihood that macroscopic rates will be controlled by growth rather than by coverage, we have decided to refer to the growth regime for the following calculations of rate constants to be passed to the larger scale model.

The saturation indexes β of CH and $CaCO_3$, shown in Fig. 14, were computed from the composition of the solution during the growth regime, i.e., between 800 and 2000 s of simulated carbonation. The β of

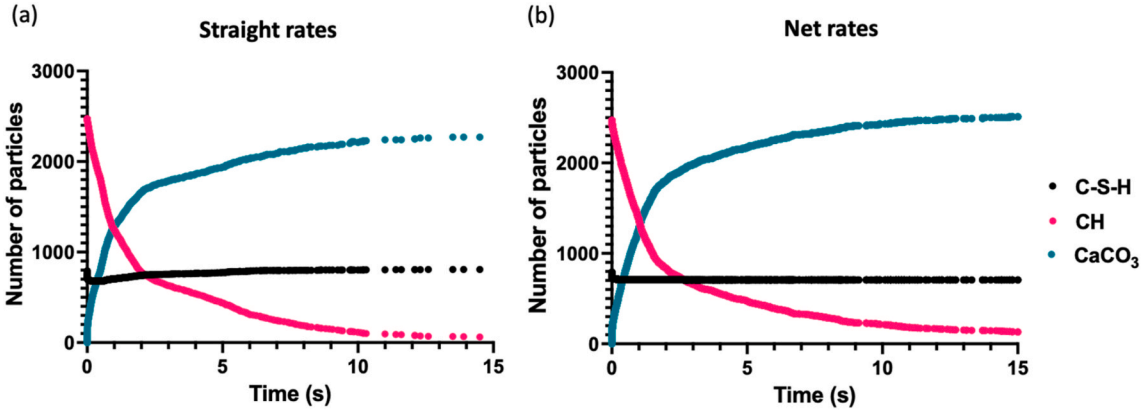

Fig. 11. Number of particles during small-box preliminary simulations, comparing the kinetics emerging from the use of (a) straight rates and (b) net rates.

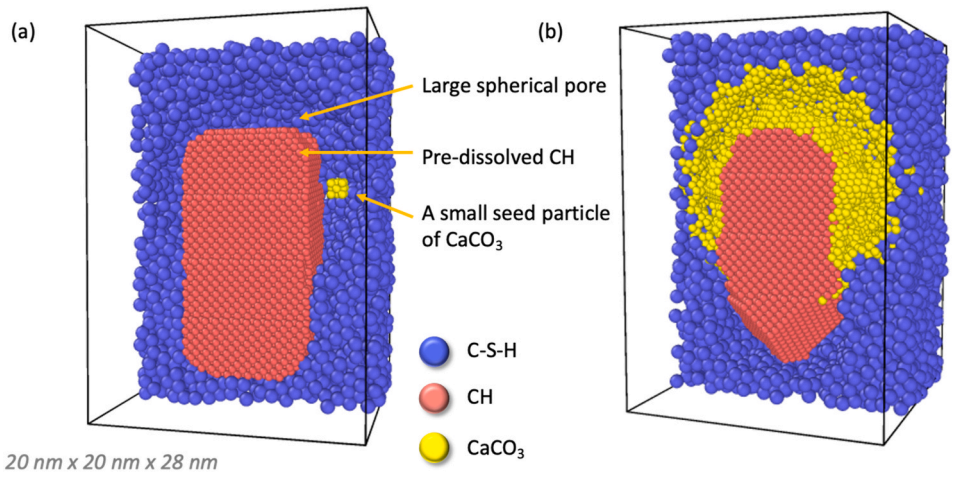

Fig. 12. Precipitation of $CaCO_3$ into a relatively large spherical pore. (a) A small seed of $CaCO_3$ is also placed in the large pore to investigate whether and to what extent it might impact growth. The simulation cell is sliced to provide a better view of (b) the growth of $CaCO_3$ into the large pore.

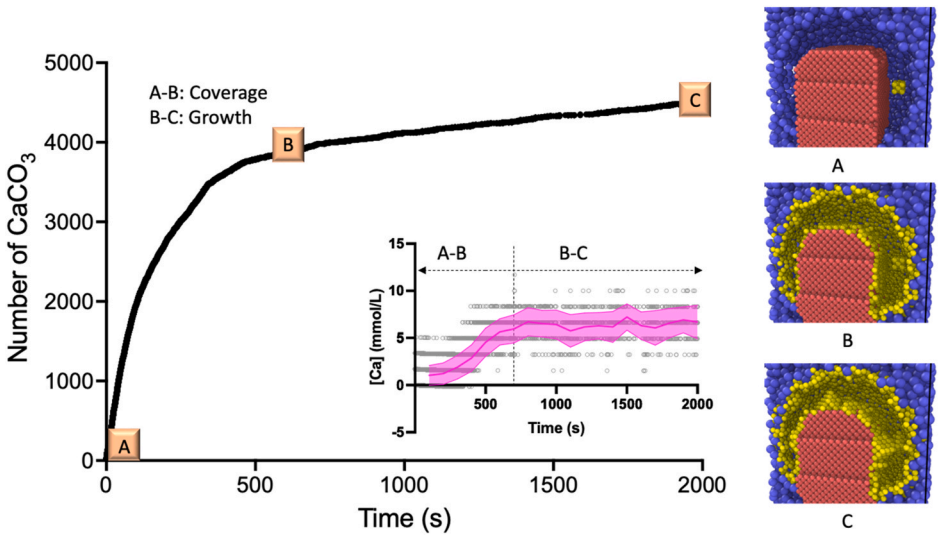

Fig. 13. $CaCO_3$ precipitation curve, displaying two distinct regimes of coverage and growth. The inset shows the evolution of the concentration of Ca ions in solution during the simulation. The pink shaded envelope shows the mean and standard deviation of the scattered concentration data points. (For interpretation of the references to colour in this figure legend, the reader is referred to the Web version of this article.)

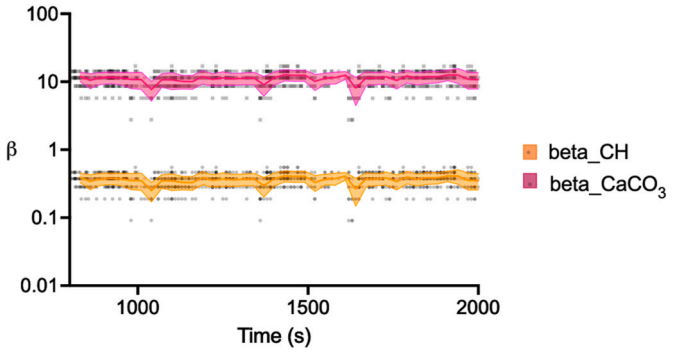

Fig. 14. Solution properties in the growth regime. The shaded envelopes show the mean and standard deviation of the scatter plot.

calcite averages around 10, and for CH it is around 0.3. Both these values are far from equilibrium ($\beta = 1$), thus neither CH dissolution nor $CaCO_3$ precipitation are rate-controlling; instead, both contribute in commensurable ways to establishing the steady state kinetics of the system. This is conceptually similar to the simulation results in Bullard et al. [61] on alite hydration, with neither dissolution nor diffusion being rate-controlling per se.

3.3. Obtaining effective rate constants for the macroscale simulations

The calculation of effective rate constants for macroscale simulations is based on analytically fitting the simulation results through the two rate equations below, which are the same as the macroscale Equations (14) and (15) except that water saturation is unit in the MASKE simulations:

$$r_{Ca(OH)2} = k_{Ca(OH)2}\left(1 - \beta_{Ca(OH)2}\right) \tag{24}$$

$$r_{CaCO3} = -k_{CaCO3}\left(1 - \beta_{CaCO3}\right) \tag{25}$$

We start with a first assumption for the values of the rate constants. Initial values of β are calculated for CH and $CaCO_3$ using the concentration of ions in the first step of the simulation, their charges, and the equilibrium constant $K_{eq,diss}$ of CH and $CaCO_3$ as described in the

methodology. With all these values, a suitably small time-step is used to perform a first integration step of the rate Equations (24) and (25), yielding an updated, analytically predicted number of CH and $CaCO_3$ particles, as well as the accompanying change in number of predicted Ca^{2+} ions in solution (the rest of the ion concentrations being fixed as in the simulations). With the updated composition of the solution, new values of β are computed prompting a new advance in time, and so forth until covering the total simulated time. All this produces analytically predicted curves for the temporal evolution of the number of CH and $CaCO_3$ particles in the system, as well as Ca^{2+} ions in solution. These curves are compared to the simulated ones during the calcite growth regime, and the analytical integration of the rate Equations (24) and (25) is repeated with new values for the rate constants until a satisfactory match (minimum least square error) between analytical and simulated results is reached. The final values of k obtained in this way were $k_{Ca(OH)2} = 2.20 \times 10^{-5}$ kg/m^3/s and $k_{CaCO3} = 4.24 \times 10^{-6}$ kg/m^3/s, which produce the fits in Fig. 15. These values of effective rate constants were then supplied to the reactive transport model to estimate the depth of penetration of carbonation. This multi-scale approach of supplying the effective rates obtained from the molecular scale model to the reactive transport model at higher scale is due to the size limitation of our particle coarse graining (i.e., 1 particle = 1 molecule). If our model is coarse-grained to higher scale (say 1 particle = 1 μm) the results from the simulation can be directly compared with experimental data.

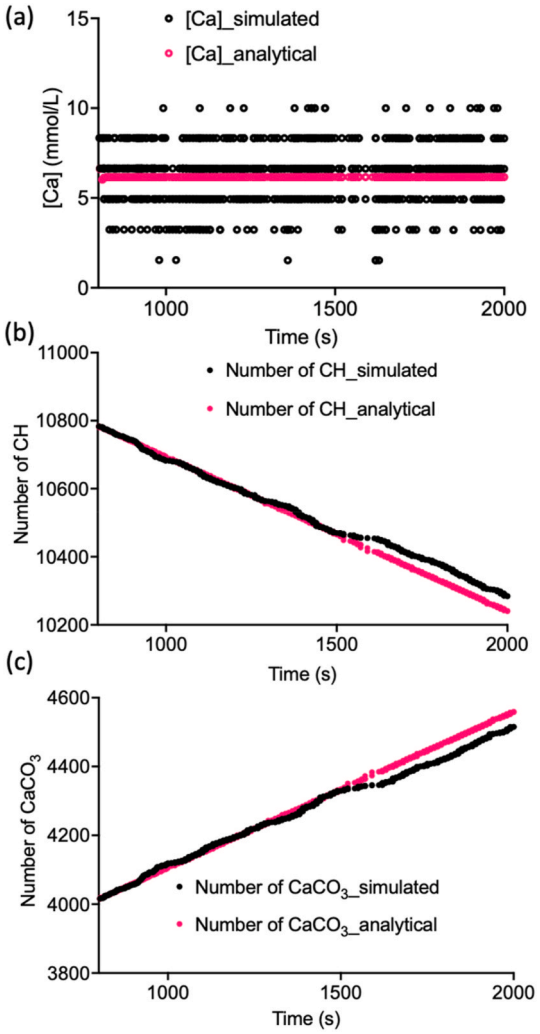

Fig. 15. Comparison between (a) MASKE-simulated vs analytical [Ca] and number of particles of (b) CH and (c) $CaCO_3$.

3.4. Bottom-up informed macroscale simulations

3.4.1. Carbonation of lime mortar

The validity of the model and upscaling procedure are demonstrated through an example problem concerning the carbonation of a non-hydraulic lime mortar, presented in Lawrence et al., 2006 [29]. The mortar samples were cured for 7 days at a relative humidity (RH) of 90%, followed by a reduction to an RH of 60% prior to testing. The samples were then left at 60% RH and exposed to an atmospheric carbon concentration of 0.035%, for 180 days, with measurements of the carbonation depth being taken at 14, 28, 90 and 180 days exposure time, using both thermogravimetric analysis, TGA, and a phenolphthalein indicator. For the numerical simulation, one-dimensional reactive transport of carbon from the environment was considered, the degree of saturation of the sample was assumed uniform at 29.28%, and the initial concentration of $Ca^{2+}(aq)$ was calculated assuming an initial chemical equilibrium (with respect to CH dissolution) based on an initial pH of 12.5. It is noted that the initial concentration is similar to the steady state value from the MASKE simulations (see Fig. 14(a)). The samples were assumed to be fully cured prior to the carbonation test such that the hydration reaction was complete, and aging was due solely to the carbonation processes. The model parameters can be seen in Table 4, except the rate constants for CH dissolution and $CaCO_3$ precipitation, that were taken from the MASKE simulations and computed in Section 3.3 above. The finite element mesh used an element size of 0.1 mm, whilst the time step size was 360 s.

A comparison between the numerical predictions and the experimental data can be seen in Fig. 16. The predicted profiles of $Ca(OH)_2(s)$ and $CaCO_3(s)$, in addition to the pH profile estimated using the empirical relation in Equation (15), can be seen in Fig. 17. The model predictions compare well with the experimental data after both 14 and 28 days. In addition, the chemical favourability of $CaCO_3(s)$ precipitation is clear, with almost all of the $Ca(OH)_2(s)$ being dissolved in the carbonated region.

3.4.2. Sensitivity of the macroscale simulations on the reaction rate constants

The example problem presented is governed by both chemical species transport and carbonation reactions. To assess the confidence level in the upscaled rate constants, we investigate the effect the rates have on the results shown in Fig. 16. To this end, the example problem was simulated with the rate constants increased and decreased by an order of magnitude respectively. The results of the investigation can be seen in Fig. 18, where Num – Upper and Num – Lower indicate the results with rate constants increased and decreased by a factor 10 respectively.

The profiles at 14 days show that there is a significant disagreement between the simulation predictions and the experimental data when the lower rates are used. Increasing the rate constants above the values obtained from MASKE, instead, does not change the resulting curves of penetration depth. Larger rate constants for CH dissolution and $CaCO_3$ carbonation make the problem increasingly transport-controlled; the rate-limiting effect of transport also increases with time, as indeed at 28 days in Fig. 18. Also the simulation results with lower rate end up coinciding with those with higher rates. It is possible therefore that we

Table 4
Model Parameters for macroscale simulations of reactive transport.

Parameter	Value	Parameter	Value
n (%)	28.20 [29]	K_H (mol/L.Patm)	3.40×10^{-2} [62]
S_l (%)	29.28 [29]	$Ca(OH)_2^{init}(s)$ (mol/L)	3.36 [29]
$D^{mol}_{Ca^{2+}}$ (m^2/s)	0.79×10^{-11} [63]	$Ca^{2+,init}(aq)$ (mol/L)	6.48×10^{-3} (based on pH = 12.5)
$D^{mol}_{CO_2}$ (m^2/s)	1.60×10^{-8} [63]	$CO_2^{init}(g)$ (%)	0.00 [29]

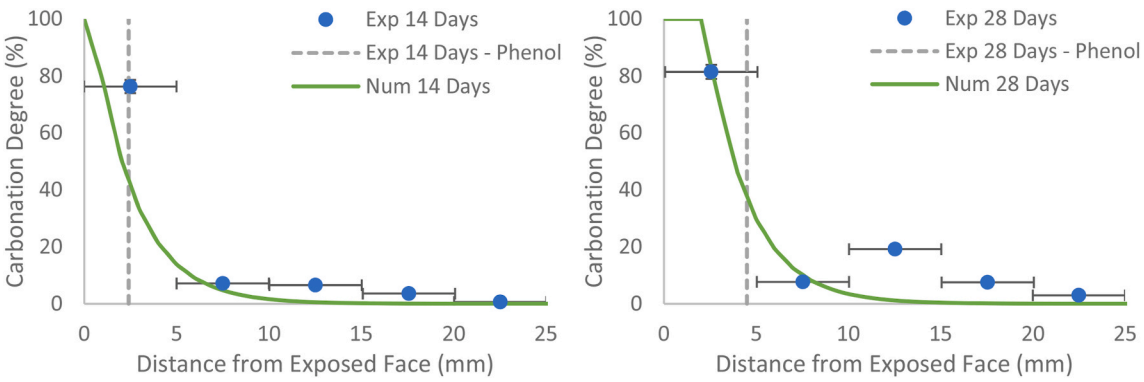

Fig. 16. Comparison of simulated carbonation profiles (Num in the legend) and the experimental data of Lawrence et al. (2006) presented in the Introduction.

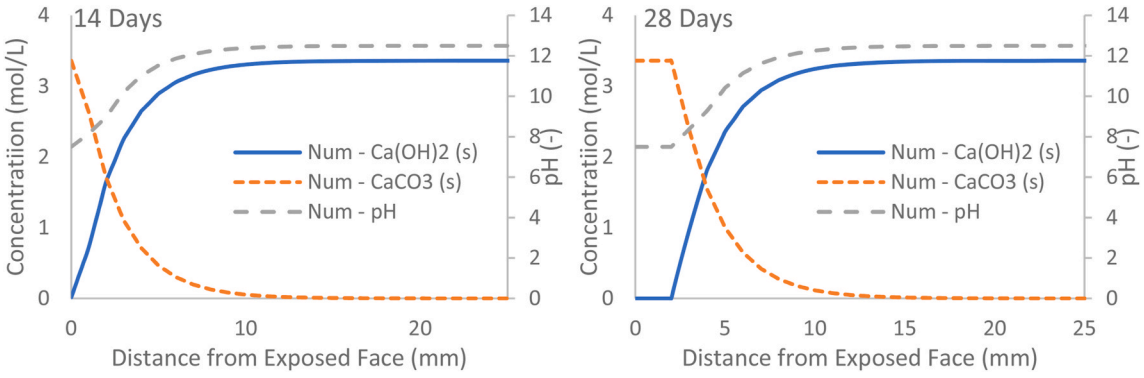

Fig. 17. Simulated profiles of $Ca(OH)_2(s)$, $CaCO_3(s)$ and estimated pH (Equation (15)).

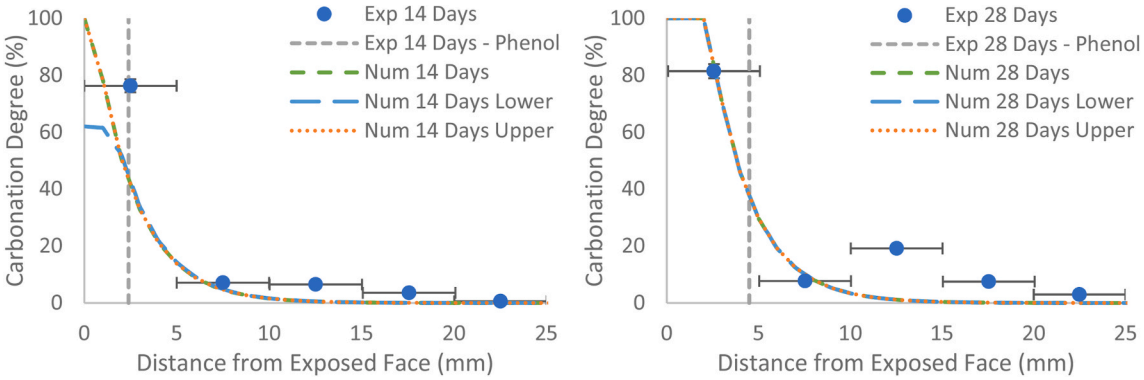

Fig. 18. Predicted carbonation profiles with altered rate constants and the results of Lawrence et al. (2006).

would have seen a greater difference between the MASKE-informed and the increased rates if we considered the carbonation profile after 7 days only.

All in all, Fig. 18 shows that the magnitude of the rate constants does play a role, but that transport also impacts the rates significantly in the example considered here. This however is not the case in general since transport sometimes is far from being rate-controlling, e.g. in carbonation when cracks are present (which is always true for self-healing problems). The presence of cracks leads to rates of transport that are orders of magnitude higher than in an intact material. This has been shown in Wang et al. (1997) [64] where the permeability coefficient for a matrix containing cracks of 0.3 mm width, was found to be 10^4 times higher than that of an intact matrix (and even higher still when the specimen was unloaded). In this case the transport is unlikely to be rate limiting and the reaction rates would need to be accurately captured, not simply "fast enough" as the results in Fig. 17 might suggest at first sight.

3.4.3. Comparison to rates in the literature

To further investigate the validity of the upscaled rate constants, the reaction rates were also compared to those reported in the literature. To this end several reaction models were considered and the reaction rates calculated for given chemical conditions. A direct comparison of rate constants is not possible because different models adopt different functional forms for the dissolution and precipitation reactions, some merging the two together into a single effective reaction; however a comparison of overall rates for similar if not identical chemical environments is possible. The dissolution reaction of Papadakis et al. (1991) [65], assuming a volume fraction of aqueous film on the pore walls of 1, a BET specific surface area of 6.2 m^2/g (Phung et al., 2016) [56], and substituting in values given in (Papadakis et al., 1991) [65] is given by:

$$r_{diss} = a_1 k_{diss}^{pap}\left([OH^-(aq)]_{eq} - [OH^-(aq)]\right) \tag{26}$$

where $a_1 = 27605$. The precipitation reaction, assuming a temperature of 298 K, is given by:

$$r_{prec} = a_2 k_{prec}^{pap} [OH^-(aq)]_{eq} [CO_2(g)] \quad (27)$$

where $a_2 = 0.836$. The initial carbonation reaction rate considered by Van Balen and Van Gemert (1994) [66], assuming no effect of saturation, is given by:

$$r_{carb} = k_{carb}^{vanb} [CO_2(g)] \quad (28)$$

A similar reaction was considered by Li et al. (2020) [67]:

$$r_{carb} = k_{carb}^{li} [Ca(OH)_2(aq)] [CO_2(g)] \quad (29)$$

Chen et al. (2019) [68]:

$$r_{carb} = k_{carb}^{chen} [OH^-(aq)]_{eq} [CO_2(aq)] \quad (30)$$

and Talukdar et al. (2012) [69]:

$$r_{carb} = k_{carb}^{taluk} [Ca(OH)_2(aq)] [CO_2(aq)] \quad (31)$$

The reactions rates in the present work are given by Equations (14) and (15), with the degree of saturation (S_l) set to 1.

Fig. 19 shows a comparison of the reaction rates predicted by the various methods; the parameters used in the comparison can be seen in Table 5. The saturation indexes β of the solid species were taken as the average values from the MASKE simulations (see Section 3.2, Fig. 13), whilst the ion concentrations in solution were chosen to be consistent with said β values. The reaction rates in this work are well within the range of those predicted using models from the literature: see Fig. 19. The $Ca(OH)_2$ dissolution and $CaCO_3$ precipitation rates do not coincide because, in the macroscale simulations, there is also a term of Ca^{2+}(aq) transport contributing to the rate balance at steady state. Specifically, in the carbonation problem, the consumption of Ca^{2+}(aq) by the precipitation reaction leads to both further dissolution of $Ca(OH)_2$(s) due to the reduction in $\beta_{Ca(OH)2}$ and transport of Ca^{2+}(aq) from the intact part of the specimen to the reaction site (i.e. in the opposite direction to the CO_2(g) transport). As a result, the precipitation is balanced by both the dissolution and the flux of Ca^{2+}(aq) ions and as such, the average values of β at steady in the macroscale simulations generally differs from the steady-state β from the MASKE simulations, shown in Fig. 17 and Table 5, as no transport is simulated at the microscale in MASKE.

3.4.4. Self-healing of cracks

To demonstrate the validity of the upscaled rate constants and BNG model for crack filling, an example problem concerning the self-healing of cracks in mortar specimens, presented in Van Tittelboom et al. [70], is

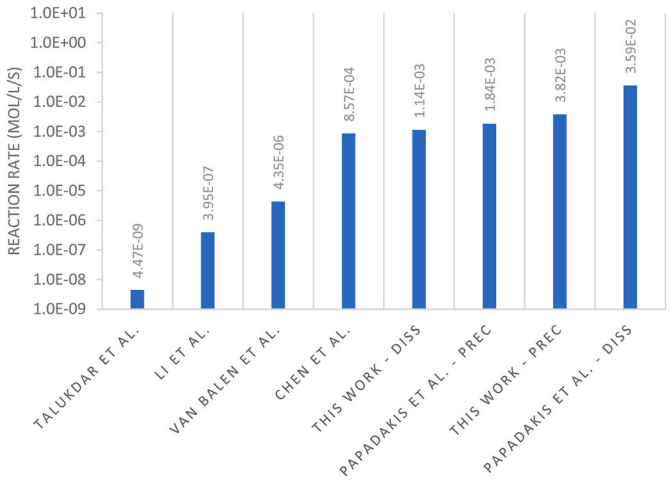

Fig. 19. Reaction rates predicted by various models.

Table 5
Parameters used in the comparison.

Species Concentrations/ Saturations	Value	Rate Constants	Value
$[OH^-(aq)]_{eq}$	43 (mmol/l)	k_{diss}^{pap}	5×10^{-5} (m/s)
$[OH^-(aq)]$	17 (mmol/l)	k_{prec}^{pap}	8.3 (m^3/mol/s)
$[CO_2(g)]$	0.00616 (mmol/l)	k_{carb}^{vanb}	0.7062 (1/s)
$[CO_2(aq)]$	0.00511 (mmol/l)	k_{carb}^{li}	9.9×10^{-3} (m^3/mol/s)
$[Ca(OH)_2(aq)]$	6.48 (mmol/l)	k_{carb}^{chen}	3.9 (m^3/mol/s)
$\beta_{Ca(OH)2}$	0.3 (-)	k_{carb}^{taluk}	1.35×10^{-4} (m^3/mol/s)
β_{CaCO3}	10 (-)		

considered. Mortar samples of dimension 160x40 × 40 mm were cured for 28 days at an RH of >95%, before being subjected to cracking in a three-point bending test. Following this, the cracked samples were immersed in tap water for a period of 1–42 days, at which times the crack widths were measured using a stereo microscope. The crack self-healing ratio was given as the reduction in crack width over the healing period, whilst the healing product was reported to be $CaCO_3$. For the numerical simulation, the BNG model reported in Section 2.5 was employed; whilst the healing of a 62.5μm crack was considered for the comparison. The model parameters can be seen in Table 6. The linear growth rate G_0, was calculated from molecular scale equation for rate constants (Equation (5),(6)) as described in methodology, and is in good agreement with values found in the literature [60,71], whilst the number of nuclei per unit surface area N_s, was assumed to be $10 \times 10^3/mm^2$, which again, is in agreement with values found in the literature [71]. The initial solution saturation index ($\beta_{CaCO3}^{initial}$) was taken as the average value from the MASKE simulations (see Section 3.2, Fig. 13). Bullard et al. [60] showed that the growth of a product layer with high opacity (which is a measure of the effect of surface coverage on inhibiting the dissolution that produces reactants and rate of transport of those reactants), leads to a rapid decrease in the solution saturation index (see Fig. 6 in Bullard et al. [60]). To account for this, we employ the following exponential function:

$$\beta_{CaCO3}(t) = \beta_{CaCO3}^{initial} e^{-Ct} + \beta_{CaCO3}^{final} (1 - e^{-Ct}) \quad (32)$$

where $C = 5.9 \times 10^{-6}\ s^{-1}$ is a constant and β_{CaCO3}^{final} is the final saturation index, taken here to be near to 1.

The comparison of the predictions of the BNG model with the experimental values can be seen in Fig. 20. It can be seen from the figure that the BNG model is in good agreement with the experiment.

3.5. Effect of interfacial energy

Section 2.2 discussed how solid-solid interfacial energies, which are controlled by the κ_{12} parameters in our MASKE simulations, are important in determining the chemo-mechanical behaviour of the system. The values of κ_{12} are generally not known; atomistic simulations might help estimating them but they will still involve large uncertainties, whereas direct experimental assessment is currently beyond capability. Hence a small study into the sensitivity of our results on κ_{12} is provided here. Thus far this work has assumed $\kappa_{12} = 0.5$ for all solid-

Table 6
Parameters used in the BNG model.

Parameter	Value
G_0 (mm/s)	2.0×10^{-8}
N_s (1/mm^2)	10×10^3
$\beta_{CaCO3}^{initial}$ (-)	10
β_{CaCO3}^{final} (-)	1.01

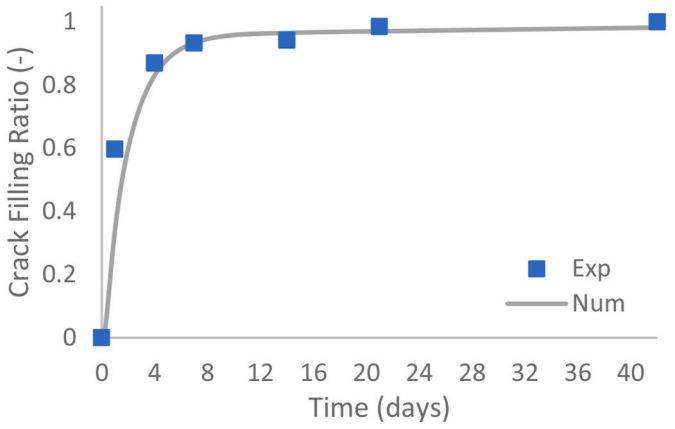

Fig. 20. Comparison of predicted self-healing of 62.5μm crack with experimental data from Van Tittelboom et al. [70].

solid interfaces between different solid species; this means that the solid-solid interfacial energy is the average of the water-solid energies of the two dissimilar particles coming in contact. The ideal way to determine this value would be to run rigorous reactive atomistic simulations between the dissimilar solid surfaces. Even such simulations may not give reliable values because atomistic simulations usually come with huge uncertainties. Thus, we go with the guess here and perform a study on how a variation in these values can influence the microstructure and mechanical properties of the final structure.

This choice of κ_{12} can have an important effect on mechanisms, such as the relative prevalence of coverage and growth. For instance, $\kappa_{12} = 0.5$ produces both a coverage and a growth regime, whereas a significantly smaller $\kappa_{12} = 0.05$ between C-S-H and $CaCO_3$ and between CH and $CaCO_3$ (i.e. unfavourable interactions between them, since the interfacial energies determines the interaction strength ε_{12} as per Equation (11)) would hinder the precipitation of calcite on C-S-H and CH surfaces, thus yielding to prevalent growth around the pre-placed calcite seed as shown in Fig. 21. Both simulations with $\kappa_{12} = 0.5$ and $\kappa_{12} = 0.05$ led to comparable reaction rates during the growth-dominated regimes, as expected since growth depends only on calcite-calcite interactions, viz. on the calcite-water interfacial energy which was the same in both simulations in Fig. 21.

The parameter κ_{12} also impacts the mechanical properties of the system. Fig. 22(b) shows an initially intact model paste of CH and C-S-H akin to the one used in this work to simulate carbonation. The paste is cracked in Fig. 22(b), simply by deleting all particles from a thin slice at mid height. Carbonation is then simulated until complete healing, leading to the systems in Fig. 22(d). Here we show only the initial and final fully precipitated state of the system. However, the comparison of stress-strain curves at different time intervals before attaining full dissolution-precipitation are presented in the conference paper [72]. The stress-strain curves in Fig. 22(a) were then computed by imposing a progressive elongation of the periodic simulation box in the vertical direction, and minimizing the interaction energy in the system. The curves in Fig. 22(a) are both for the intact system in Fig. 22(b) and for the healed system in Fig. 22(d), but for this latter we considered two cases: one with CH-C-S-H and CH-$CaCO_3$ interactions dictated by $\kappa_{12} = 0.5$, the other one with $\kappa_{12} = 0.05$. Expectedly, the stronger inter-phase forces sustained by $\kappa_{12} = 0.5$ lead to healed system that is even stiffer and stronger in tension than the original intact paste; however, this is contrary to the experimental observations, where strength recovery in healed systems is usually partial at best. The stress-strain curves for $\kappa_{12} = 0.05$ instead display a more realistic loss of strength compared to the intact system. Thus, getting an accurate estimate of interfacial energy is important to correctly predict both the precipitation mechanisms and the mechanical performance of carbonated systems and, more in general, of any system with chemically heterogeneous microstructures; this warrants further studies in the future.

4. Conclusions

The Kinetic Monte Carlo (KMC) model in this work successfully simulated the 3D evolution of microstructure during carbonation, while tracking information on the evolving solution chemistry and of the mechanical interactions between phases controlling the overall evolution of mechanical properties of the system. The following conclusions emerged:

- During carbonation, the simulations correctly predict that CH dissolves providing a constant supply of ions for $CaCO_3$ to precipitate, while the amount of C-S-H in the system remains approximately constant despite it is in principle allowed to dissolve or precipitate indefinitely.
- Simulations using straight rate expressions are knowingly more accurate than simulations using net rates, but the latter are significantly more efficient (~2.5 times faster) and were shown to produce similar dissolution-precipitation profiles and overall rates in regimes where rapid fluctuations between dissolution and precipitation events are not critical to morphology evolution (in particular during coverage and growth, as opposed to initial nucleation).
- The calcite precipitation curves show two distinct regimes of (i) coverage and (ii) growth, during which the predicted concentration

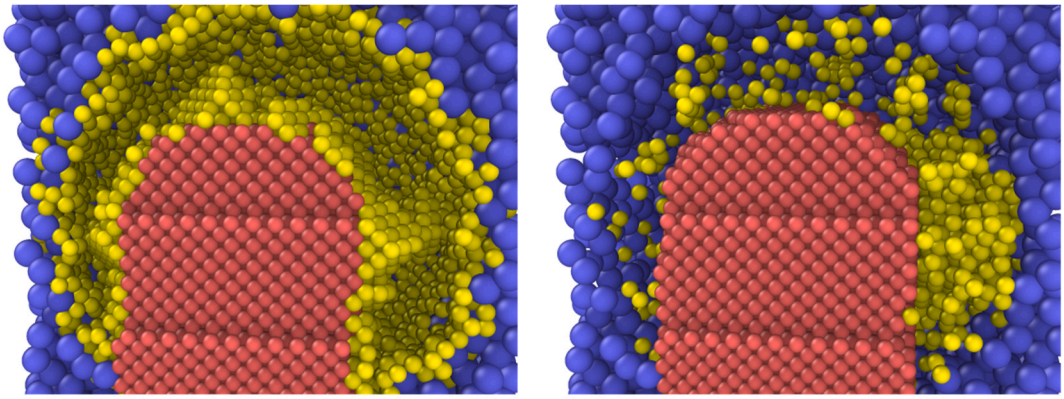

Fig. 21. Varying the interaction potential through κ_{12} between C-S-H-CaCO3 and CH-CaCO3. Coverage and growth were observed for (a) $\kappa_{12} = 0.5$ whereas predominant growth from the calcite seed was obtained with (b) $\kappa_{12} = 0.05$.

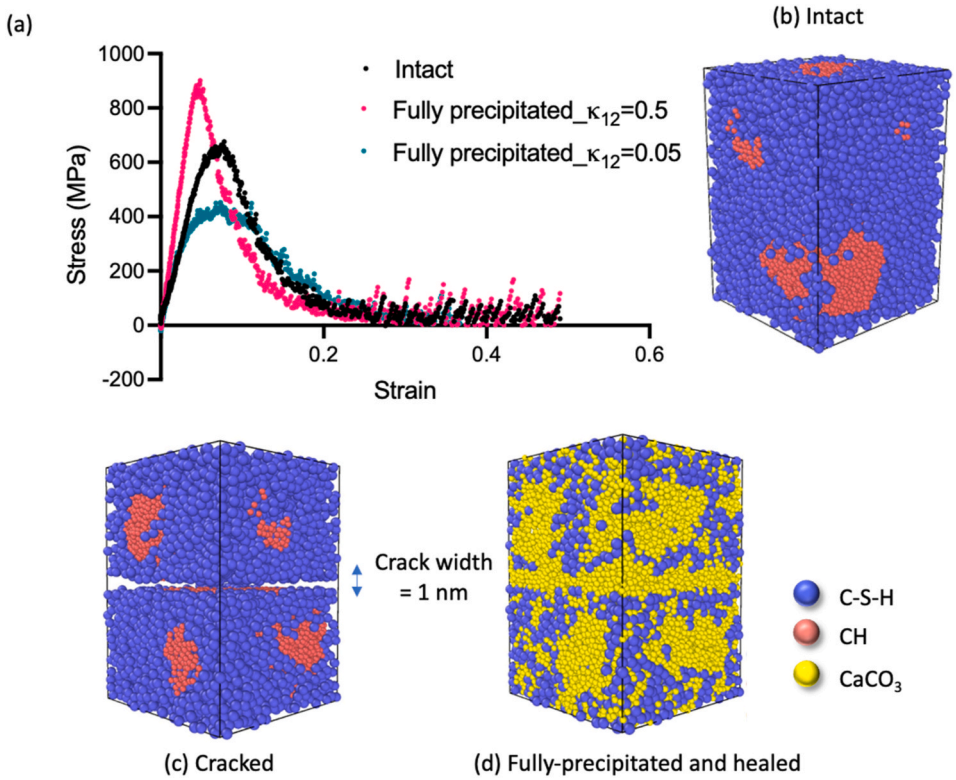

Fig. 22. (a) Stress-strain plots of intact vs fully precipitated with $\kappa_{12} = 0.5$ and $\kappa_{12} = 0.05$, (b) intact system with C-S-H and CH, (c) cracked with a crack width of 1 nm, (d) fully precipitated system with calcite bridging the crack.

of calcium ions in solution remains in the order of few mmol/L, in good agreement with expected values from the literature.

- The values of saturation indexes $\beta_{Ca(OH)2}$ and β_{CaCO3} predicted by the KMC simulations were both far from unity, meaning that neither CH dissolution nor $CaCO_3$ precipitation were rate-controlling during steady-state carbonation.
- Effective reaction rate constants for CH dissolution and carbonate precipitation were derived from the KMC simulations, with reference to the carbonate growth regime. These constants, applied to a reactive transport model at the macroscale, provided a satisfactory prediction of carbonation depth profiles as from experiments in Lawrence et al. [29]. Reaction rates estimated for CH dissolution and $CaCO_3$ precipitation were also within the range reported in various works in the literature.
- The molecular reaction rate for $CaCO_3$ precipitation, when applied to a new boundary nucleation and growth model, provided a satisfactory prediction of self-healing of a crack from experiments in Van Tittelboom et al. [70].
- An expression is proposed to estimate the interaction energy between solid particles of dissimilar species and dissimilar size, all based on a single parameter κ_{12} that determines the solid-solid interfacial energy between the species. κ_{12} is a significant parameter affecting the morphology and mechanical performance of the system. The bulk of the results in this manuscript refer to a choice of $\kappa_{12} = 0.5$, but dedicated simulations with other values of κ_{12} showed that the rate in the growth regime (hence the effective rates passed to the macroscale model) did not depend significantly on κ_{12}, since the carbonate growth regime depends on CH-CH interactions rather than interactions between CH and other solid phases. Further investigations are required to obtain an accurate value of κ_{12}.

The work in this paper can now be extended in several directions. The method presented here can be immediately used to improve the mechanistic hypotheses underlying the macroscale models of carbonation, also beyond the expressions of reaction rate constants addressed in this work. At the microscopic scale, then, further insight can be gained into the values of κ_{12} or, more in general, of solid-solid interfacial energies and interaction energies between particles of dissimilar species. This would likely entail a combination of bottom-up efforts starting from atomistic simulations, and top-down parameter optimization targeting experimental results at larger length scales.

Another desirable development is to further the coarse-graining beyond the one-particle = one-molecule level chosen here. Pushing the coarse-graining to micrometre-sized particles, for example, would allow simulating the chemo-mechanical evolution of microstructures at a length scale where direct comparison with experimental results is possible, e.g., from imaging techniques. The micro-to-millimetre scale is also the appropriate one to apply the presented approach to the engineering challenge of designing microbial-self-healing concretes [23]. On the other hand, coarser graining requires modifications to the unimolecular rate equations in this work, and one would have to make assumptions on the molecular-scale mechanisms of nucleation, growth, and dissolution that the coarse-grained rate equations will consider implicitly: e.g., see Shvab et al. [33]. In this regard, having started from an unimolecular coarse graining here provides a good starting point to devise reasonable mechanistic assumptions to be used in following studies with coarse graining.

Finally, even with the minimal coarse graining adopted here, the proposed method is readily available to study systems with different chemical compositions and coupled chemo-mechanical processes other than carbonation, such as dissolution-precipitation at grain boundaries, interaction between minerals and admixtures, or degradation induced by pressure solution or crystallization pressure [52]. The system can also be used to study the crack filling effects of other forms of calcium carbonate (e.g., vaterite and aragonite) provided the chemo-mechanical input parameters are available for those forms. All in all, this work has demonstrated how chemo-mechanical, particle-based, KMC simulations at the microscale can predict the evolution of morphology,

mechanical properties, and reaction rates during carbonation and carbonation based self-healing of concrete, all of which can be used to inform macroscale models thus reducing their reliance on heuristic constitutive assumptions that limit their predictive ability. This provides a new avenue to support the current endeavours towards a simulation-assisted management of degradation of both traditional and innovative cementitious materials.

Funding

This work was funded by EPSRC Standard Grant Engineering MICP via meso-Scale Simulations (Newcastle University EP/S013997/1; University of Bath EP/S013857/1; Cardiff University EP/S01389X/1).

Declaration of competing interest

The authors declare that they have no known competing financial interests or personal relationships that could have appeared to influence the work reported in this paper.

Data availability

The data files are available at DOI: http://doi.org/10.17035/d.2023.0252928416

References

[1] S. von Greve-Dierfeld, B. Lothenbach, A. Vollpracht, B. Wu, B. Huet, C. Andrade, C. Medina, C. Thiel, E. Gruyaert, H. Vanoutrive, I.F. Saéz del Bosque, I. Ignjatovic, J. Elsen, J.L. Provis, K. Scrivener, K.C. Thienel, K. Sideris, M. Zajac, N. Alderete, Ö. Cizer, P. Van den Heede, R.D. Hooton, S. Kamali-Bernard, S.A. Bernal, Z. Zhao, Z. Shi, N. De Belie, Understanding the carbonation of concrete with supplementary cementitious materials: a critical review by RILEM TC 281-CCC, Materials and Structures/Materiaux et Constructions 53 (2020), https://doi.org/10.1617/s11527-020-01558-w.

[2] Y. Chen, P. Liu, Z. Yu, Effects of environmental factors on concrete carbonation depth and compressive strength, Materials 11 (2018), https://doi.org/10.3390/ma11112167.

[3] M. Moreno, W. Morris, M.G. Alvarez, G.S. Duffó, Corrosion of reinforcing steel in simulated concrete pore solutions effect of carbonation and chloride content, Corrosion Sci. 46 (2004) 2681–2699, https://doi.org/10.1016/j.corsci.2004.03.013.

[4] E. Gruyaert, P. van den Heede, N. de Belie, Carbonation of slag concrete: effect of the cement replacement level and curing on the carbonation coefficient - effect of carbonation on the pore structure, Cem. Concr. Compos. 35 (2013) 39–48, https://doi.org/10.1016/j.cemconcomp.2012.08.024.

[5] D. Zhang, Y. Shao, Effect of early carbonation curing on chloride penetration and weathering carbonation in concrete, Construct. Build. Mater. 123 (2016) 516–526, https://doi.org/10.1016/j.conbuildmat.2016.07.041.

[6] H. Ye, X. Jin, C. Fu, N. Jin, Y. Xu, T. Huang, Chloride penetration in concrete exposed to cyclic drying-wetting and carbonation, Construct. Build. Mater. 112 (2016) 457–463, https://doi.org/10.1016/j.conbuildmat.2016.02.194.

[7] M. Zajac, J. Skocek, P. Durdzinski, F. Bullerjahn, J. Skibsted, M. ben Haha, Effect of carbonated cement paste on composite cement hydration and performance, Cement Concr. Res. 134 (2020), https://doi.org/10.1016/j.cemconres.2020.106090.

[8] H. El-Hassan, Y. Shao, Carbon storage through concrete block carbonation, Journal of Clean Energy Technologies (2014) 287–291, https://doi.org/10.7763/jocet.2014.v2.141.

[9] J. Skocek, M. Zajac, M. ben Haha, Carbon Capture and Utilization by mineralization of cement pastes derived from recycled concrete, Sci. Rep. 10 (2020), https://doi.org/10.1038/s41598-020-62503-z.

[10] K. Akimoto, F. Sano, J. Oda, H. Kanaboshi, Y. Nakano, Climate change mitigation measures for global net-zero emissions and the roles of CO2 capture and utilization and direct air capture, Energy and Climate Change 2 (2021), 100057, https://doi.org/10.1016/j.egycc.2021.100057.

[11] J.G. Jang, G.M. Kim, H.J. Kim, H.K. Lee, Review on recent advances in CO2 utilization and sequestration technologies in cement-based materials, Construct. Build. Mater. 127 (2016) 762–773, https://doi.org/10.1016/j.conbuildmat.2016.10.017.

[12] D. Ravikumar, D. Zhang, G. Keoleian, S. Miller, V. Sick, V. Li, Carbon dioxide utilization in concrete curing or mixing might not produce a net climate benefit, Nat. Commun. 12 (2021), https://doi.org/10.1038/s41467-021-21148-w.

[13] At Least 8% of Global Emissions Caused by Humans Come from the Cement Industry Alone.", n.d..

[14] V. Wiktor, H.M. Jonkers, Quantification of crack-healing in novel bacteria-based self-healing concrete, Cem. Concr. Compos. 33 (2011) 763–770, https://doi.org/10.1016/j.cemconcomp.2011.03.012.

[15] J.A. Rosewitz, S. Wang, S.F. Scarlata, N. Rahbar, An enzymatic self-healing cementitious material, Appl. Mater. Today 23 (2021), https://doi.org/10.1016/j.apmt.2021.101035.

[16] K. Van Tittelboom, N. De Belie, Self-healing in cementitious materials-a review, Materials 6 (2013) 2182–2217, https://doi.org/10.3390/ma6062182.

[17] B. Sharma, A. Singh, S. Joshi, M.S. Reddy, Utilization of sandstone waste in cement mortar for sustainable production of building materials through biomineralization, J Sustain Cem Based Mater 12 (2023) 712–720, https://doi.org/10.1080/21650373.2022.2116500.

[18] C. Qian, X. Yu, T. Zheng, Y. Chen, Review on bacteria fixing CO2 and bio-mineralization to enhance the performance of construction materials, J. CO2 Util. 55 (2022), 101849, https://doi.org/10.1016/j.jcou.2021.101849.

[19] X. Yu, H. Rong, Seawater based MICP cements two/one-phase cemented sand blocks, Appl. Ocean Res. 118 (2022), 102972, https://doi.org/10.1016/j.apor.2021.102972.

[20] B. Sharma, A. Singh, S. Joshi, M.S. Reddy, Utilization of sandstone waste in cement mortar for sustainable production of building materials through biomineralization, J Sustain Cem Based Mater 12 (2023) 712–720, https://doi.org/10.1080/21650373.2022.2116500.

[21] R. Garg, R. Garg, N.O. Eddy, Microbial induced calcite precipitation for self-healing of concrete: a review, J Sustain Cem Based Mater 12 (2023) 317–330, https://doi.org/10.1080/21650373.2022.2054477.

[22] X. Yu, Q. Zhang, Microbially/CO_2-derived $CaCO_3$ cement and its microstructural and mechanical performance, J Sustain Cem Based Mater 12 (2023) 1156–1168, https://doi.org/10.1080/21650373.2023.2178539.

[23] M. Bagga, C. Hamley-Bennett, A. Alex, B.L. Freeman, I. Justo-Reinoso, I.C. Mihai, S. Gebhard, K. Paine, A.D. Jefferson, E. Masoero, I.D. Ofiţeru, Advancements in bacteria based self-healing concrete and the promise of modelling, Construct. Build. Mater. 358 (2022), 129412, https://doi.org/10.1016/j.conbuildmat.2022.129412.

[24] V.G. Papadakis, M.N. Fardis, C.G. Vayenas, Effect of Composition, Environmental Factors and Cement-Lime Mortar Coating on Concrete Carbonation, 1992.

[25] A. v Saetta, B.A. Schrefler, R. v Vitaliani, The Carbonation of Concrete and the Mechanism of Moisture, Heat and Carbon Dioxide Flow through Porous Materials, 1993.

[26] H.F.W. Taylor, Cement Chemistry, 20, Academic Press, 1990, p. 335, https://doi.org/10.1016/S0958-9465(98)00023-7.

[27] A.S. Chitez, A.D. Jefferson, A coupled thermo-hygro-chemical model for characterising autogenous healing in ordinary cementitious materials, Cement Concr. Res. 88 (2016) 184–197, https://doi.org/10.1016/j.cemconres.2016.07.002.

[28] B.L. Freeman, P.J. Cleall, A.D. Jefferson, An indicator-based problem reduction scheme for coupled reactive transport models, Int. J. Numer. Methods Eng. 120 (2019) 1428–1455, https://doi.org/10.1002/nme.6186.

[29] R.M.H. Lawrence, T.J. Mays, P. Walker, D. D'Ayala, Determination of carbonation profiles in non-hydraulic lime mortars using thermogravimetric analysis, Thermochim. Acta 444 (2006) 179–189, https://doi.org/10.1016/j.tca.2006.03.002.

[30] A. Funk, H.F.R. Trettin, DFT study on the effect of water on the carbonation of portlandite, Ind. Eng. Chem. Res. 52 (2013) 2168–2173, https://doi.org/10.1021/ie302972k.

[31] S.M. Mutisya, A.G. Kalinichev, Carbonation reaction mechanisms of portlandite predicted from enhanced ab initio molecular dynamics simulations, Minerals 11 (2021), https://doi.org/10.3390/min11050509.

[32] K. Ioannidou, C. Labbez, E. Masoero, A review of coarse grained and mesoscale simulations of C–S–H, Cement Concr. Res. 159 (2022), https://doi.org/10.1016/j.cemconres.2022.106857.

[33] I. Shvab, L. Brochard, H. Manzano, E. Masoero, Precipitation Mechanisms of Mesoporous Nanoparticle Aggregates: Off-Lattice, Coarse-Grained, Kinetic Simulations, Coarse-Grained, Kinetic Simulations, 17, Crystal Growth & Design, 2017, https://doi.org/10.1021/acs.cgd.6b01712i.

[34] K. Coopamootoo, E. Masoero, Simulations of crystal dissolution using interacting particles: prediction of stress evolution and rates at defects and application to tricalcium silicate, J. Phys. Chem. C 124 (2020) 19603–19615, https://doi.org/10.1021/acs.jpcc.0c04633.

[35] F. Lolli, H. Manzano, J.L. Provis, M.C. Bignozzi, E. Masoero, Atomistic simulations of geopolymer models: the impact of disorder on structure and mechanics, ACS Appl. Mater. Interfaces 10 (2018) 22809–22820, https://doi.org/10.1021/acsami.8b03873.

[36] T.Z. Forbes, A.V. Radha, A. Navrotsky, The energetics of nanophase calcite, Geochem. Cosmochim. Acta 75 (2011) 7893–7905, https://doi.org/10.1016/j.gca.2011.09.034.

[37] E. Ruiz-Agudo, K. Kudłacz, C.V. Putnis, A. Putnis, C. Rodriguez-Navarro, Dissolution and carbonation of portlandite [Ca(OH)2] single crystals, Environ. Sci. Technol. 47 (2013) 11342–11349, https://doi.org/10.1021/es402061c.

[38] F.H. Wittmann, Estimation of the modulus of elasticity of calcium hydroxide, Cement Concr. Res. 16 (1986) 971–972, https://doi.org/10.1016/0008-8846(86)90021-9.

[39] C. Estrela, C.R.deA. Estrela, L.F. Guimarães, R.S. Silva, J.D. Pécora, Surface tension of calcium hydroxide associated with different substances, J. Appl. Oral Sci. 13 (2005) 152–156, https://doi.org/10.1590/S1678-77572005000200011.

[40] E. Masoero, J.J. Thomas, H.M. Jennings, A reaction zone hypothesis for the effects of particle size and water-to-cement ratio on the early hydration kinetics of C3S, J. Am. Ceram. Soc. 97 (2014) 967–975, https://doi.org/10.1111/jace.12713.

[41] E. Masoero, G. Di Luzio, Nanoparticle simulations of logarithmic creep and microprestress relaxation in concrete and other disordered solids, Cement Concr. Res. 137 (2020), https://doi.org/10.1016/j.cemconres.2020.106181.
[42] J.W. Bullard, G.W. Scherer, J.J. Thomas, Time dependent driving forces and the kinetics of tricalcium silicate hydration, Cement Concr. Res. 74 (2015) 26–34, https://doi.org/10.1016/j.cemconres.2015.03.016.
[43] J. Ekprasert, I. Fongkaew, P. Chainakun, R. Kamngam, W. Boonsuan, Investigating mechanical properties and biocement application of CaCO3 precipitated by a newly-isolated Lysinibacillus sp. WH using artificial neural networks, Sci. Rep. 10 (2020), 16137, https://doi.org/10.1038/s41598-020-73217-7.
[44] H.M. Jennings, Aqueous solubility relationships for two types of calcium silicate hydrate, J. Am. Ceram. Soc. 69 (1986) 614–618, https://doi.org/10.1111/j.1151-2916.1986.tb04818.x.
[45] F. Wang, Y. Liu, S. Hu, Effect of early cement hydration on the chemical stability of asphalt emulsion, Construct. Build. Mater. 42 (2013) 146–151, https://doi.org/10.1016/j.conbuildmat.2013.01.009.
[46] V. Gogulancea, R. González-Cabaleiro, B. Li, D. Taniguchi, P.G. Jayathilake, J. Chen, D. Wilkinson, D. Swailes, A.S. McGough, P. Zuliani, I.D. Ofiteru, T. P. Curtis, Individual based model links thermodynamics, chemical speciation and environmental conditions to microbial growth, Front. Microbiol. 10 (2019), https://doi.org/10.3389/fmicb.2019.01871.
[47] B. Lothenbach, D.A. Kulik, T. Matschei, M. Balonis, L. Baquerizo, B. Dilnesa, G. D. Miron, R.J. Myers, Cemdata18: a chemical thermodynamic database for hydrated Portland cements and alkali-activated materials, Cement Concr. Res. 115 (2019) 472–506, https://doi.org/10.1016/j.cemconres.2018.04.018.
[48] J.W. Bullard, A three-dimensional microstructural model of reactions and transport in aqueous mineral systems, Model. Simulat. Mater. Sci. Eng. 15 (2007) 711–738, https://doi.org/10.1088/0965-0393/15/7/002.
[49] J.W. Bullard, G.W. Scherer, J.J. Thomas, Time dependent driving forces and the kinetics of tricalcium silicate hydration, Cement Concr. Res. 74 (2015) 26–34, https://doi.org/10.1016/j.cemconres.2015.03.016.
[50] A Compilation of Rate Parameters of Water-Mineral Interaction Kinetics for Application to Geochemical Modeling, (n.d).
[51] Ö. Cizer, C. Rodriguez-Navarro, E. Ruiz-Agudo, J. Elsen, D. Van Gemert, K. Van Balen, Phase and morphology evolution of calcium carbonate precipitated by carbonation of hydrated lime, J. Mater. Sci. 47 (2012) 6151–6165, https://doi.org/10.1007/s10853-012-6535-7.
[52] E. Masoero, MASKE: particle-based chemo-mechanical simulations of degradation processes, in: RILEM Bookseries, Springer Science and Business Media B.V., 2023, pp. 159–170, https://doi.org/10.1007/978-3-031-33211-1_15.
[53] H.M. Jennings, A model for the microstructure of calcium silicate hydrate in cement paste 30 (2000) 101–116.
[54] H.M. Jennings, J.J. Thomas, J.S. Gevrenov, G. Constantinides, F.-J. Ulm, A multi-technique investigation of the nanoporosity of cement paste, Cement Concr. Res. 37 (2007) 329–336, https://doi.org/10.1016/j.cemconres.2006.03.021.
[55] C.M. Turley, S. Widdicombe, Literature Review: Environmental Impacts of a Gradual or Catastrophic Release of CO2 into the Marine Environment Following Carbon Dioxide Capture CoastWEB View Project Sea Turtle Conservation View Project, 2004. https://www.researchgate.net/publication/294685308.
[56] Q.T. Phung, N. Maes, D. Jacques, G. De Schutter, G. Ye, J. Perko, Modelling the carbonation of cement pastes under a CO2 pressure gradient considering both diffusive and convective transport, Construct. Build. Mater. 114 (2016) 333–351, https://doi.org/10.1016/j.conbuildmat.2016.03.191.
[57] J. Article Author, ETH Library Corrosion of steel in carbonated concrete: mechanisms, practical experience, and research priorities-a critical review by RILEM TC 281-CCC, (n.d.). https://doi.org/10.3929/ethz-b-000456483.
[58] C.F. Chang, J.W. Chen, The experimental investigation of concrete carbonation depth, Cement Concr. Res. 36 (2006) 1760–1767, https://doi.org/10.1016/j.cemconres.2004.07.025.
[59] E. Masoero, Mesoscale mechanisms of cement hydration: BNG model and particle simulations, in: Handbook of Materials Modeling, Springer International Publishing, 2020, pp. 177–197, https://doi.org/10.1007/978-3-319-44680-6_149.
[60] J.W. Bullard, G.W. Scherer, J.J. Thomas, Time dependent driving forces and the kinetics of tricalcium silicate hydration, Cement Concr. Res. 74 (2015) 26–34, https://doi.org/10.1016/j.cemconres.2015.03.016.
[61] J.W. Bullard, H.M. Jennings, R.a. Livingston, A. Nonat, G.W. Scherer, J. S. Schweitzer, K.L. Scrivener, J.J. Thomas, Mechanisms of cement hydration, Cement Concr. Res. 41 (2011) 1208–1223, https://doi.org/10.1016/j.cemconres.2010.09.011.
[62] J. Jeong, H. Ramézani, E. Chuta, Reactive transport numerical modeling of mortar carbonation: atmospheric and accelerated carbonation, J. Build. Eng. 23 (2019) 351–368, https://doi.org/10.1016/j.jobe.2019.01.038.
[63] L. Li, M.H. Hubler, Y. Xi, Theoretical modeling on chemical composition and mechanical properties of well cement under carbonation reactions, J. Clean. Prod. 276 (2020), https://doi.org/10.1016/j.jclepro.2020.124270.
[64] K. Wang, D.C. Jansen, S.P. Shah, A.F. Karr, PI1 SOOOS-8846(97)00031-8 PERMEABILITY STUDY OF CRACKED CONCRETE, 1997.
[65] Fundamental modeling and experimental investigation of concrete carbonation, ACI Mater. J. 88 (1991), https://doi.org/10.14359/1863.
[66] K. Van Balen, D. Van Gemert, Modelling lime mortar carbonation, Mater. Struct. 27 (1994) 393–398, https://doi.org/10.1007/BF02473442.
[67] L. Li, M.H. Hubler, Y. Xi, Theoretical modeling on chemical composition and mechanical properties of well cement under carbonation reactions, J. Clean. Prod. 276 (2020), https://doi.org/10.1016/j.jclepro.2020.124270.
[68] T. Chen, X. Gao, L. Qin, Mathematical modeling of accelerated carbonation curing of Portland cement paste at early age, Cement Concr. Res. 120 (2019) 187–197, https://doi.org/10.1016/j.cemconres.2019.03.025.
[69] S. Talukdar, N. Banthia, J.R. Grace, Carbonation in concrete infrastructure in the context of global climate change - Part 1: experimental results and model development, Cem. Concr. Compos. 34 (2012) 924–930, https://doi.org/10.1016/j.cemconcomp.2012.04.011.
[70] K. Van Tittelboom, E. Gruyaert, H. Rahier, N. De Belie, Influence of mix composition on the extent of autogenous crack healing by continued hydration or calcium carbonate formation, Construct. Build. Mater. 37 (2012) 349–359, https://doi.org/10.1016/j.conbuildmat.2012.07.026.
[71] E. Masoero, J.J. Thomas, H.M. Jennings, A reaction zone hypothesis for the effects of particle size and water-to-cement ratio on the early hydration kinetics of C3S, J. Am. Ceram. Soc. 97 (2014) 967–975, https://doi.org/10.1111/jace.12713.
[72] A. Alex, E. Masoero, Autogenous healing in cement: a kinetic Monte Carlo simulation of CaCO3 precipitation, in: Computational Modelling of Concrete and Concrete Structures, CRC Press, 2022, pp. 102–106, https://doi.org/10.1201/9781003316404-12.